



LAWRENCE
LIVERMORE
NATIONAL
LABORATORY

Uncertainty quantification of material parameters in modeling coupled metal and high explosive experiments

M. D. Nelms, W. Schill, I. W. Kuo, N. R. Barton, K. Schmidt

May 24, 2024

Journal of Applied Physics

Disclaimer

This document was prepared as an account of work sponsored by an agency of the United States government. Neither the United States government nor Lawrence Livermore National Security, LLC, nor any of their employees makes any warranty, expressed or implied, or assumes any legal liability or responsibility for the accuracy, completeness, or usefulness of any information, apparatus, product, or process disclosed, or represents that its use would not infringe privately owned rights. Reference herein to any specific commercial product, process, or service by trade name, trademark, manufacturer, or otherwise does not necessarily constitute or imply its endorsement, recommendation, or favoring by the United States government or Lawrence Livermore National Security, LLC. The views and opinions of authors expressed herein do not necessarily state or reflect those of the United States government or Lawrence Livermore National Security, LLC, and shall not be used for advertising or product endorsement purposes.

9 Abstract

10 Experiments involving the coupling of metal and high explosives (HE) are of notable defense-
11 related interest, and we seek to refine the uncertainty quantification associated with models
12 of such experiments. In particular, our focus is on how uncertainty related to the metal
13 constitutive model challenges our ability to infer high explosive model parameters when
14 analyzing focused science experiments. We consider three focused experiments involving an
15 HE accelerating metal: small plate tests with tantalum/LX-14 and tantalum/LX-17 pairings
16 as well as a tantalum/LX-17 cylinder test. For all three models, we perform sensitivity
17 analysis to ascertain the influence of metal strength on the coupled experimental response.
18 Moreover, we calibrate each model in a Bayesian setting and study the quantification of metal
19 strength on the inference of the HE parameters. Based on our results, we offer guidance for
20 future metal/HE experiments.

21 1 Introduction

22 Accurate calibration and assessment of associated uncertainty for equation of state (EOS)
23 models related to energetic material detonation is of significant interest to the defense com-
24 munity for a wide variety of applications. The main challenge of calibrating these models
25 emanates from complex physical chemistry underlying the chemical phase change occurring
26 during the detonation process, particularly in high explosives (HE)[1]. Performing focused
27 experiments often requires a coupling between the HE and a metal; here, the metal facilitates
28 experimental measurement of the free surface velocity, which aids in the modeling of the HE
29 [1–3]. When modeling such experiments, this coupling between the two material types can
30 potentially introduce additional uncertainty given the complex loading conditions imparted
31 on the metal and the underlying complexity of accurately modeling metal strength. The
32 constitutive model related to the metal strength will often require formulations that include
33 rate, temperature, and pressure dependence as well as porosity nucleation and growth.

34 Our goal is to quantify the response uncertainty of the coupled metal/HE experiments.
35 Of particular interest is the degree to which uncertainty in the metal strength model affects
36 the uncertainty of the experimental response as well as the inferred HE parameters. We
37 employ Monte Carlo error propagation to assess the impact of metal strength uncertainty
38 on the experimental response uncertainty, and we use sensitivity analysis to identify the
39 most significant parameters in the models of coupled experiments. Both the metal strength
40 parameters and the HE parameters of such models are estimated using Bayesian inference,
41 which naturally quantifies the associated uncertainty.

42 We consider two types of coupled metal/HE experiments: small plate tests and cylinder
43 tests. We consider small plate tests using either LX-14[3] and LX-17 HE [2] as well as a
44 cylinder test using LX-17 HE[1]. LX-14 and LX-17 are two commonly-used HE materials,
45 and analyzing experiments with both types of HE provides a comparison between a sensitive

46 and insensitive HE, respectively. To leverage previous work in the statistical modeling of
47 material strength, we focus on using tantalum as the metal component in each of these
48 experiments. While tantalum has been well studied, modeling it across a wide range of
49 pressure, temperature, strain rate, and strain conditions has proven to be quite challenging
50 [4–6].

51 Recently the *Schill et al.* [7] studied tantalum strength using Bayesian analysis and
52 compared pulsed power and gas gun experiments. For a discussion of specific physical effects
53 that accompany release of material from the compressed state, see [8–11]. For a more general
54 application of calibration methods in problems of dynamic compression of condensed matter,
55 we suggest [12–20]. More broadly, similar methodology has been applied in high energy
56 density physics [21–27] as well as computational plasticity [28, 29].

57 Sensitivity analysis of experiments involving tantalum have also been previously studied
58 [7, 30, 31]. [7] and [31] specifically consider sensitivity of tantalum strength parameters. As
59 shown in [31], the strength parameter sensitivity differs by experimental regime.

60 The literature available on HE model calibration and uncertainty using statistical in-
61 ference is limited, but it does provide some useful resources. Higdon *et al.* [32] calibrated
62 energy-related parameters for an HE of interest in an cylinder expansion test using Bayesian
63 inference. They found that the determination of the HE model parameters was challenging
64 with limited experiments. In Lee *et al.* [33], they calibrated EOS models for a variety of HEs
65 to rate-stick experiments. In Andrews & Fraser [34], they employed a Bayesian approach
66 to verify that an HE EOS could be recovered using synthetic data. This work provides a
67 basis to assess the effects of a metal constitutive model on our ability to infer HE model
68 parameters. Additionally, Andrews *et al.* [35] applied Bayesian calibration to the Davis
69 Products EOS model for PBX 9501 while Lindquist *et al.* [36] calibrated the reactant and
70 product forms of the Davis EOS to a variety of conventional HE materials.

71 We leverage this existing work to analyze the uncertainty of coupled metal/HE experi-
72 ments and unlike previous studies we include uncertainty of the metal strength model pa-
73 rameters. The outline of this study is as follows. In Section 2, we describe the metal/HE
74 experimental configurations. The modeling of these experiments is discussed in Section 3.
75 Section 4 gives an overview of the statistical methodology. Implementation of these methods
76 and their results are presented in Section 5. In Section 6, we provide conclusions, including
77 experimental recommendations based on our analysis.

78 2 Coupled Metal/HE Experiments

79 In this section, we describe the small plate and cylinder experimental configurations. In both
80 cases, tantalum is chosen for the metal component. Data collected from the experimental
81 setups described below can be found in [1–3]. The first experimental configuration considered
82 in this investigation is the small plate test. In this experiment, a thin disc of high explosive

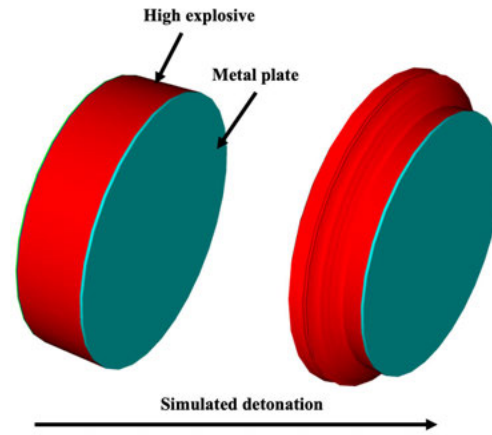


Figure 1: Small plate computational model where the high explosive pushes a thin metal plate during detonation.

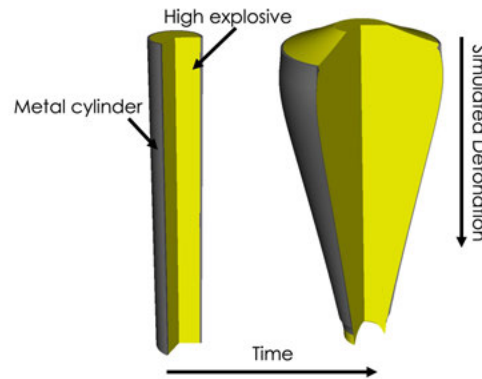


Figure 2: Cylinder test computational model where a metal cylinder confines a high explosive and expands the metal during the detonation.

83 material is pressed against a thin plate of metal. (See Figure 1). We modeled two types of
 84 HE: sensitive (LX-14) and insensitive (LX-17). In either case, the detonation of the chosen
 85 HE pushes a tantalum plate, and the free surface velocity is measured using Fabry-Perot
 86 interferometry.

87 The cylinder test is a calibrated pipe bomb designed to give detonation energies by
 88 measuring the free-surface velocity. The HE is ignited at one end of the cylinder with the
 89 velocity measurement taking place at approximately $2/3$ of the total length assuming steady
 90 detonation has been achieved. In this case, the velocimetry is performed using Fabry-Perot
 91 interferometry. The expansion process of the metal cylinder is visualized in Figure 2.

92 A summary of the experiments and the salient details can be found in Table 1. The small
 93 plate experiments were chosen due to the relatively *thick* tantalum plates which increases the

94 likelihood that spall will convolute the ability to infer HE model parameters. Additionally,
 95 the small plate configuration are experiments with large HE and metal diameters which
 96 allows us to neglect 2-D effects until relatively late times. Lastly, the tests are *historical* in
 97 the sense they are experiments that were performed using methods and data reporting that
 98 was not as detailed as it would be with modern experimental methods. The following analysis
 99 will allow us to assess the efficacy of *historical* experiments when calibrating modern HE
 100 models by assessing the effects of variance on as-reported measurements, notably the charge
 101 thickness in plate experiments.

Table 1: Experimental dimensions and bounds for emulator training

Shot num.	Type	HE	HE Thickness or Diameter (cm)	Metal Thickness (cm)
cyl-LX-17 [1]	Cylinder	LX-17	2.5376	0.2714
smplt-LX-17[2]	Small plate	LX-17	1.5245 [1.372, 1.6775]	0.052
smplt-LX-14[3]	Small plate	LX-14	3.8995 [3.50,4.29]	0.0769

[1] Alidis *et al.*, [2] Tarver et al., and [3] Lee *et al.*

102 3 Metal/HE Experiment Modeling and Simulation

103 Due to the complexity of coupled metal/HE experiments, modeling is achieved via multi-
 104 physics simulations. In this section, we highlight components of these simulations. Consti-
 105 tutive models for the metal component are detailed in Section 3.1. A brief description of
 106 the HE model is given in Section 3.2. The simulations were performed using the LLNL hy-
 107 drocode, Ares [37]. The small plate and cylinder experiments were modeled with the metal
 108 being Lagrangian and the high explosive leveraging the code's arbitrary Lagrangian-Eulerian
 109 (ALE) capability to allow the mesh to relax at late times. The configuration was modeled
 110 as 1-D. The cylinder test was modeled with a 2-D axisymmetric representation given the ro-
 111 tational symmetry about the center axis of the cylinder. A large number of simulations were
 112 run in order to train the Gaussian process used to emulate the computationally-intensive
 113 multi-physics code. See Section 4.1 for more details related to the emulator.

114 3.1 Constitutive model descriptions

115 The experimental configurations simulated here involve HE pushing metal in two differ-
 116 ent configurations. This requires that each material have its own constitutive model with
 117 the HE model simulating the detonation process related to a phase and thermochemical
 118 change from an unreacted solid to a gaseous product and condensed detonation soot. The
 119 metal, on the other hand, is modeled with what is colloquially known as a *strength model*.
 120 Here, the strength model is comprised of a combination of an equation of state (EOS), flow

121 stress model and a porosity model for *simplt-LX-14* and *cyl-LX-17* experiments and only
 122 the Preston-Tonks-Wallace (PTW) flow stress model for *simplt-LX-17* due to challenges with
 123 coupling a porosity model and the soot parameter capability. The PTW [38] model, which
 124 is commonly used in hydrocodes, serves as our flow stress model. When porosity is included,
 125 the PTW model is coupled to porosity models, which help account for the wide range of
 126 strain rates, pressure, and temperature conditions experienced by the metal. For the follow-
 127 ing simulations, two different porosity models are used; they are described in 3.1.2. The EOS
 128 for the metal is Mie-Grüneisen in form and believed to be well understood and calibrated in
 129 the range of conditions in this study therefore is not included in the calibration.

130 3.1.1 Preston-Tonks-Wallace flow stress model

131 The PTW model is intended to be used for complex loading conditions, which include a wide
 132 range of strain rate, strain, and temperature conditions. This model is based on the Voce
 133 hardening law, and uses physically-motivated scalings of the flow stress. The PTW model
 134 includes two branches: one for modeling lower rates ($< \sim 10^5/s$) via a phenomenological
 135 depiction of the thermally-activated dislocation glide and another for modeling high rate
 136 conditions, where the form is motivated by phonon drag. The conditions predicted based
 137 on simulations using the nominal parameters predict pressures of 19 and 14 GPa and strain
 138 rates of $9 \cdot 10^5/s$ and $4 \cdot 10^5/s$ for LX-14 and LX-17, respectively. It is believed that phonon
 139 drag effects are not observed at these strain rates [39, 40]. The flow stress τ takes the form

$$\tau = 2\hat{\tau}G(P, T), \quad (1)$$

140 where $G(P, T)$ is the pressure- and temperature-dependent shear modulus and $\hat{\tau}$ is the non-
 141 dimensional shear strength given by

$$\hat{\tau} = \hat{\tau}_s + \frac{1}{p} (s_0 - \hat{\tau}_y) \ln \left[1 - \left[1 - \exp \left(-p \frac{\hat{\tau}_s - \hat{\tau}_y}{s_0 - \hat{\tau}_y} \right) \right] \exp \left(\frac{-p\theta\psi}{(s_0 - \hat{\tau}_y) \exp \left(p \frac{\hat{\tau}_s - \hat{\tau}_y}{s_0 - \hat{\tau}_y} \right)} \right) \right]. \quad (2)$$

142 Here, $\hat{\tau}_s$ and $\hat{\tau}_y$ —respectively representing the saturation and yield stress—are rate and
 143 thermal dependent. Model constants s_0 and s_∞ are the values $\hat{\tau}_s$ takes at zero Kelvin and
 144 very high temperatures. Similarly, y_0 and y_∞ are the values of the yield strength $\hat{\tau}_y$ at zero
 145 Kelvin and very high temperatures. In particular, $\hat{\tau}_s$ and $\hat{\tau}_y$ are defined as

$$\hat{\tau}_s = \max \left\{ s_0 - (s_0 - s_\infty) \operatorname{erf} \left[k\hat{T} \ln \left(\gamma\dot{\xi}/\dot{\epsilon}_p \right) \right], \min \left[y_1 \left(\dot{\epsilon}_p/\gamma\dot{\xi} \right)^{y_2}, s_{0d} \left(\dot{\epsilon}_p/\gamma\dot{\xi} \right)^\beta \right] \right\} \quad (3)$$

146 and

$$\hat{\tau}_y = \max \left\{ y_0 - (y_0 - y_\infty) \operatorname{erf} \left[k\hat{T} \ln \left(\gamma\dot{\xi}/\dot{\epsilon}_p \right) \right], s_{0d} \left(\dot{\epsilon}_p/\gamma\dot{\xi} \right)^\beta \right\}. \quad (4)$$

147 In equations (3) and (4), a modified strain rate normalization factor $\dot{\xi}$, takes the form

$$\dot{\xi} = \frac{1}{2} \left(\frac{4\pi\rho}{3M} \right)^{\frac{1}{3}} \left(\frac{G}{\rho} \right)^{\frac{1}{2}} \quad (5)$$

148 with ρ being the mass density and M denoting the molar mass.

149 A useful feature of Bayesian statistical approaches is that they make use of subject matter
150 expert knowledge. One way that knowledge comes into play is via selection of suitable ranges
151 for parameter values. The PTW model parameters and their expert-determined bounds for
152 tantalum are given in Table 2. Parameters that are not specified in the table are fixed at their
153 nominal values from [38] rather than inferred. Note that γ is sampled on the log (base 10)
154 scale when ensembles of simulation inputs are employed to cover the admissible parameter
155 space for emulator training.

Table 2: PTW model parameters, nominal values, and ranges used in calibration.

Parameter	Nominal	Calibration range	Truncated normal mean (variance)	Units
θ	0.02	[0.001, 0.05]	0.0148($1.64 \cdot 10^{-06}$)	-
p	0	[0, 10]	4.9181 (0.1039887)	-
s_0	0.012	[0.005, 0.02]	0.00514($2.08 \cdot 10^{-08}$)	-
s_∞	0.00325	[0.002, 0.006]	0.00589($6.43 \cdot 10^{-09}$)	-
κ	0.6	[0.1, 0.9]	0.727 (0.00011)	-
γ	$4 \cdot 10^{-5}$	$[-\log(10^{-3}), -\log(10^{-8})]$	$-\log(10^{5.132})(-\log(10^{0.00259}))$	-
y_0	0.01	[0.002, 0.02]	0.00956($5.83 \cdot 10^{-08}$)	-
y_∞	0.00123	[0.0005, 0.003]	0.00135($1.31 \cdot 10^{-09}$)	-
y_1	0.012	0.012	-	-
y_2	0.4	0.4	-	-
β	0.23	0.23	-	-

156 3.1.2 Porosity models

157 For simulations in which we model porosity, two different forms are employed. The first—
158 used in our modeling of the LX-14 small plate experiment—is a number-density porosity,
159 where the pore volume fraction ϕ and rate-dependent evolution $\dot{\phi}$ is a Cocks-Ashby-based
160 formulation[41, 42]. As described in [43–45], the rate sensitivity n enters directly into the
161 porosity kinetics, and the dominant term in the kinetics has the form

$$\dot{\phi} = c_1 \sinh \left[c_2 \left(\frac{n - \frac{1}{2}}{n + \frac{1}{2}} \right) \left(\frac{-p}{\tau_\phi} \right) \right] \left[\frac{1}{(1 - \phi)^n} - (1 - \phi) \right] \dot{\epsilon}_p, \quad (6)$$

162 where τ_ϕ is the flow strength evaluated at a strain rate that includes contributions from
 163 plasticity associated with porosity evolution, p is the pressure, and c_1 and c_2 are order-unity
 164 material parameters. Note that we use c_1 and c_2 as parameters in the model calibration of
 165 the LX-14 small plate configuration.

166 This porosity model is coupled to the PTW flow stress model (see Section 3.1.1), which
 167 also includes material softening due to the increase in porosity [44]. A subset of these porosity
 168 parameters are inputs to the coupled metal/HE experimental simulations; these parameters
 169 are noted in Table 3. The following additional parameters were included in the emulator
 170 training simulations and calibration: volume fraction available for stress nucleation $f_{n\alpha}^0$,
 171 calibration parameter for the strength degradation function a_1 , and the average pressure at
 172 which pores will nucleate $\sigma_{hM\alpha}$. A more complete discussion of this porosity model along with
 173 the nucleation parameters can found in Qamar *et al.* [45]. For evaluating mesh resolution
 174 effects, further work in the area could involve V& V based approaches [46].

Table 3: Number-density porosity model parameters: nominal calibration and ranges used in the calibration

Parameter	Nominal	Calibration Rang	Units
c_1	1.0	[0.5, 2.0]	-
c_2	2.0	[0.5, 2.5]	-
$f_{n\alpha}^0$	0.001	$[-\log(10^{-2}), -\log(10^{-6})]$	-
a_1	25.0	[4.0, 10.0]	-
$\sigma_{hM\alpha}$	$600 \cdot 10^{-5}$	$[100 \cdot 10^{-5}, 800 \cdot 10^{-5}]$	MBar

175 The second porosity model, used in the cylinder test simulations, is the Gurson porosity
 176 model where ϕ^* is a modified pore volume fraction that includes enhanced softening due
 177 to void coalescence. In equation 7, σ_e is the effective, or von Mises, stress Y is flow stress
 178 and P is the pressure. The parameters q_1 , traditionally set to 1.5, and q_2 , which is used
 179 in the model calibration, are yield surface parameters. Also included in the calibration is
 180 $f_{T\sigma}$ which is the volume fraction for potential stress nucleation. Table 4 defines the nominal
 181 values as well as the emulator training ranges used for calibration. Here we present only the
 182 salient equation which defines the yield surface. For additional details about the model, a
 183 full list and description of parameters, and implementation see [47]. The Gurson model is
 184 a modification of the classical von Mises yield surface, which is represented by the first two
 185 terms of:

$$\sigma_e^2 - Y^2 - Y^2 \left[2q_1 \phi^* \cosh \left(-\frac{3}{2} q_2 \frac{P}{Y} \right) + q_1^2 \phi^{*2} \right] = 0, \quad (7)$$

186 This formulation allows for the effects of voids in a ductile material with the inclusion of
 187 the third term. Taken with traditional continuum mechanics concepts one can derive the
 188 porosity evolution equation.

Table 4: Gurson porosity model parameters: nominal calibration and ranges used in the calibration

Parameter	Nominal	Calibration	Units
q_2	0.625	[0.5, 1.0]	-
$f_{T\sigma}$	0.001	$[-\log(10^{-2}), -\log(10^{-6})]$	-

189 3.2 HE Model

190 For the HE model, we used the Cheetah thermochemical code to model the detonation
191 of the two HE materials. Cheetah controls the conversion of unreacted HE materials to
192 gaseous product species through kinetic rate laws as well as solve sets of thermodynamics
193 equations to maintain instantaneous chemical equilibrium between possible product species.
194 This allows us to estimate the pressure-volume relationship necessary for the HE EOS. For
195 a more in-depth discussion of Cheetah look to [48].

196 In Table 5, we present the Cheetah model parameters and bounds used in the emulator
197 training. The different experimental configurations modeled used different combinations of
198 parameters. Choice of these parameters is detailed below.

Table 5: Cheetah model parameter bounds used for emulator training

Parameter	LX-14 small plate	LX-17 small plate	LX-17 cylinder test	Units
V_m	-	(4.0, 8.0)	-	cm^3/mol
E_{shift}	(-0.01, 0.01)	-	(-0.01, 0.004)	Mbar
P_{freeze}	(2.00e4, 2.00e5)	-	(4.00e4, 1.20e5)	atm
$chrgthk$	(3.50, 4.28)	(1.3725, 1.6775)	-	cm

199 For the LX-14 small plate configuration discussed in Section 5.1, we utilized two user
200 adjustable parameters recommended for fine tuning the HE models, namely the energy shift
201 (E_{shift}) and chemistry freeze-out pressure (P_{freeze}) parameters. The energy shift (E_{shift}) pa-
202 rameter will adjust the energy density by specified amounts. The chemistry freeze-out pres-
203 sure (P_{freeze}) represents pressure below which the Cheetah assumes no further instantaneous
204 chemical equilibrium. Additionally, the charge thickness ($chrgthk$)—or, the thickness of the
205 HE disk— are used as a parameter with appropriate bounds because the reported values
206 was an average of multiple measurements on a nonuniform disk. For the LX-17 small plate
207 configuration discussed in Section 5.2, an additional parameter controlling the molar den-
208 sity of soot formed through detonation[49] was include which is denoted as V_m . Given that
209 the LX-17 small plate data is also from historical experiments, we opt to include a charge
210 thickness parameter for the same reasons as in the LX-14 small plate calibration. Lastly,
211 we model the LX-17 cylinder test discussed in Section 5.3 with energy shift (E_{shift}) and
212 chemistry freeze-out pressure (P_{freeze}) parameters.

213 4 Overview of Statistical Methodology

214 Here, we introduce the statistical methodology applied to the models given in Section 3. In
215 particular, we describe how a Gaussian process can be used to emulate the complex multi-
216 physics models used to characterize our metal/HE experiments. We also highlight sensitivity
217 analysis, which us identifies the most influential model parameters, and Bayesian inference,
218 which is used to calibrate model parameters and quantify the associated uncertainty.

219 4.1 Gaussian Process Emulation

220 Recall that our integrated metal/HE experiments are modeled with computationally expen-
221 sive multi-physics models. For many statistical methods, a large number of model evaluations
222 are required. With such an expensive model, this is not computationally feasible. In these
223 cases, we instead utilize an emulator—which closely approximates an expensive model while
224 also being much cheaper to evaluate—in place of the original model.

225 In particular, we employ a Gaussian process regression (GPR) model as our our emulator
226 for each of our three experimental configurations (small plate tests with both LX-14 and
227 LX-17 and a cylinder test with LX-17). GPR is an attractive choice for an emulator due to
228 the built-in quantification of uncertainty introduced due to emulator approximation. Each
229 Gaussian process was implemented using the GPy package [50]. We chose a Matérn kernel
230 with $\nu = 5/2$.

231 To train each Gaussian process emulator, we performed a large number of simulations.
232 (See Table 6 for more details). These simulations were run using sets of parameters (ap-
233 propriate to the particular experiment) obtained via a Latin hypercube design bounded by
234 the ranges given in Section 3. These simulations were divided into *training* and *testing* sets.
235 The training set, consisting of parameters and simulation outputs, were used to train the
236 Gaussian process. The testing set was used to assess generalization beyond the training data.
237 The simulations conducted for emulator training consumed a non-trivial amount of compu-
238 tational resources. The 1D LX-14 simulations utilized one node (with 36 cores) for 3 minutes
239 of wall-clock run time for a total of 60k core-hours, and the 1D LX-17 simulations used a
240 similar allocation. The more computationally intensive 2D cylinder calculations utilized 168
241 cores with a run time of ~ 2 hours each, for a total of ~ 1.4 million core-hours.

242 In Figure 3, the behavior of the emulator is compared to the original simulation for the
243 LX-14 small plate configuration. This experimental condition was chosen as an exemplar for
244 assessing emulator performance. The desired behavior in such a plot is the line of slope one
245 passing through the origin, which would indicate a perfect match between the model and the
246 emulator. The tighter the grouping around this line, the better the emulator is at mimicking
247 the behavior of the original model. Note in Figure 3 that the training set and the testing
248 set exhibit similar grouping, indicating that we have not overfit. The gray region indicates
249 the estimated experimental error from Fabry-Perot interferometry.

This is the author's peer reviewed, accepted manuscript. However, the online version of record will be different from this version once it has been copyedited and typeset.
PLEASE CITE THIS ARTICLE AS DOI: 10.1063/5.0226642

Table 6: Information related to the training of each Gaussian process emulator for all experimental conditions.

Experiment Type	# Parameters	# Training Points	# Testing Points
Small Plate LX-14	16	3500	800
Small Plate LX-17	10	3500	800
Cylinder LX-17	12	2955	672

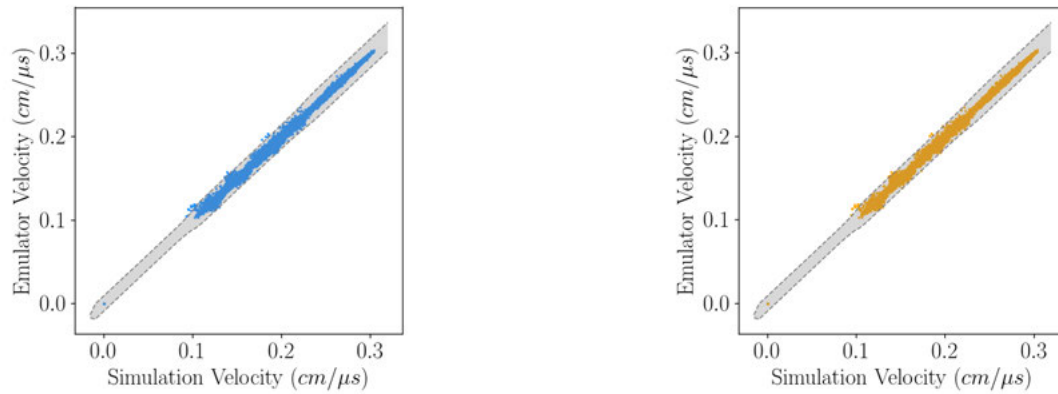


Figure 3: Plot of simulation values versus emulator prediction for (a) the training set and (b) the held-out testing set.

250 The number of simulations necessary for a well-trained emulator was first determine for
251 the LX-14 small plate experiment since had the highest dimensional parameter space and
252 then replicated for the LX-17 small plate configuration. The size of the training test was
253 determined by progressively increasing the number of simulations until the emulator training
254 and testing performance was acceptable. Due to the similarities in the velocimetry we are
255 emulating the dimensionality was the dominate consideration when determining the size of
256 the training set. A reduced training set was used for the cylinder test configuration given the
257 previously noted computationally intensive calculations. Given the emulator performance
258 was equivalent to the other configurations the number of training calculations was determined
259 to be sufficient.

260 4.2 Sensitivity Analysis

261 In sensitivity analysis, the variation (or, uncertainty) in a model response is proportioned to
262 variation in each of the input variables (i.e., parameters). The goal of this type of analysis is
263 to ascertain which parameters have the greatest impact on the model response. Sensitivity
264 analysis techniques can be categorized as either local or global. Local sensitivity analysis
265 quantifies the change in model output when the parameters are perturbed about a nomi-
266 nal value—e.g., using partial derivatives evaluated at a particular point. Global sensitivity
267 analysis characterizes parameter influence throughout the entire range of possible parame-
268 ter values (i.e. the admissible parameter space). We employ Sobol' indices, a measure of
269 global sensitivity, for our analysis. See [19] for more information of Sobol' indices and their
270 computation.

271 Standard Sobol' indices, as described in [19], are used for models with scalar responses.
272 For each of our experimental conditions, our model response is functional—namely, measured
273 velocity over time. We instead employ a functional version of Sobol' indices as in [30, 31].
274 This allows us to assess how the parameter sensitivity evolves over time. Note that the
275 calculation of Sobol' indices requires a large number of model evaluations, so we use an
276 emulator, as described in Section 4.1, for computational efficiency.

277 4.3 Bayesian Inference

278 We seek to calibrate the metal strength and HE parameters of each experimental model and
279 quantify the associated uncertainty. To achieve this, we employ Bayesian calibration. In
280 the Bayesian framework, parameters are random variables with their probability densities
281 reflecting the current state of knowledge about their values. These densities are constructed
282 using both prior information and experimental data. Model parameters $\boldsymbol{\theta} = [\theta_1, \theta_2, \dots, \theta_p]$
283 are inferred from experimental data $\mathbf{y} \in \mathbb{R}^m$ by applying Bayes' Theorem

$$\pi(\boldsymbol{\theta}|\mathbf{y}) = \frac{\mathcal{L}(\mathbf{y}|\boldsymbol{\theta})\pi_0(\boldsymbol{\theta})}{\int_{\mathbb{R}^p} \mathcal{L}(\mathbf{y}|\boldsymbol{\theta})\pi_0(\boldsymbol{\theta})}, \quad (8)$$

284 where π is the posterior density, \mathcal{L} is the likelihood function, π_0 is the prior distribution, and
285 p is the number of model parameters to be calibrated. The goal of Bayesian calibration is
286 to construct the posterior distribution $\pi(\boldsymbol{\theta}|\mathbf{y})$, and the width of the posterior characterizes
287 the parameter uncertainty.

288 In addition to the experimental data, information encoded in the prior distribution π_0 also
289 affects the parameter inference from (8). The prior distribution is chosen in such a way to
290 reflect any previous knowledge about the model parameters (e.g., physical constraints, expert
291 knowledge, or previous experiments). Note that information from previous experiments can
292 only be used in the prior if you do not reuse the previous data in the current calibration (via
293 the likelihood function).

294 Experimental data is incorporated in Bayesian inference through the likelihood function,
295 denoted as \mathcal{L} in (8). Here, $\mathcal{L}(\mathbf{y}|\boldsymbol{\theta})$ quantifies the likelihood of observing measurements \mathbf{y} given
296 model parameters $\boldsymbol{\theta}$. An appropriate likelihood function is derived from a combination of
297 the physics model and an error model for the statistical noise. See [19] for more details.

298 As stated above, the goal of Bayesian calibration is to obtain the posterior density defined
299 by (8). Despite the seemingly-straightforward formulation, computation of the posterior is
300 often difficult in practice. Due to the normalizing integral in the denominator, an analytic
301 form of the posterior exists only in special cases [19]. We instead utilize Markov chain
302 Monte Carlo (MCMC) to obtain a posterior distribution. Since we cannot analytically
303 represent $\pi(\boldsymbol{\theta}|\mathbf{y})$, Markov chain Monte Carlo (MCMC) is employed to generate a sequence
304 of samples from the posterior distribution. In particular, we use pyMC 2.3.8 to facilitate
305 adaptive Metropolis MCMC sampling. The PTW model includes constraints on parameters
306 as defined in [46]. For the Bayesian calibration, constraints were enforced in the likelihood
307 function. In practice, this was done in the code by assigning very small likelihood outputs
308 to parameter inputs violating the constraints. This will lead to them being rejected during
309 the acceptance/rejection stage of the Metropolis algorithm and not being included in the
310 posterior.

311 To perform Bayesian calibration via MCMC, a large number of model evaluations are
312 required. The exact number required is problem dependent, and in this case required 1.2^6
313 model calls. If this were performed through hydrocode simulations it would take over 60,000
314 wall-clock hours, or ~ 7 years, for the small plate and over two million wall-clock hours,
315 or 273 years, for the cylinder tests. By leveraging the emulator, we can perform the same
316 calibration in less than 2 hours. Thus, we employ a Gaussian process emulator as described
317 in section 4.1.

318 5 Implementation and Results

319 While the previous section introduced the statistical concepts, here, we give details on the
320 implementation of our analysis. We first train a Gaussian process emulator as described in

321 Section 4.1. Next, we employ this emulator for Monte Carlo error propagation to ascertain
322 how the metal flow stress affects the experimental response. We then perform sensitivity
323 analysis followed by Bayesian inference.

324 Monte Carlo error propagation allows us to qualitatively assess the effect of parameter
325 uncertainty on the uncertainty of the model response. We employ a distribution, corre-
326 sponding to model input uncertainty, from which we draw parameters. We draw a large
327 number of parameter values and use each of these resulting parameter sets to evaluate the
328 model, giving an ensemble of model predictions. Due to the computational expense, we
329 utilize our Gaussian process emulator. The width of the ensemble spread characterizes the
330 model uncertainty attributed to the input uncertainty.

331 To assess the impact of *well-characterized*, the PTW strength model parameters on the
332 model response uncertainty, we performed Monte Carlo error propagation with all three
333 experimental configurations. By *well-characterized* we mean a robust calibration to low-
334 cost experiments such as quas-static and Kolsky bar experiments as well as possibly an
335 additional high strain rate, large strain experiment such as Taylor cylinder test. Focusing
336 on the flow stress component of the model, we fixed all other parameters to the mean values
337 of the samples used for training the Gaussian process emulator. For all three metal/HE
338 experiments, we employed 500 parameter draws from two different distributions for the
339 eight PTW parameters: a truncated uniform distribution (with each parameter sampled
340 independently) bounded by the ranges in Table 2 and a posterior distribution obtained from
341 a previous calibration of the PTW model to mechanical testing data. The calibration data
342 set included stress-strain measurements from [51] (corrected in [52]) and Taylor cylinder
343 impact data from [52]. Note that this posterior distribution is narrower than the bounded
344 flat distribution; moreover, the parameters drawn from the posterior are not necessarily
345 independent.

346 After ascertaining the qualitative influence of the metal flow stress parameters, we em-
347 ployed sensitivity analysis to quantify the relative influence of the full parameter set in all
348 three experimental models. As introduced in Section 4.2, we used Sobol' indices to perform
349 sensitivity analysis on models with functional output. Numerical calculation of the Sobol'
350 indices was done via Saltelli's method. (See [19] for more information). This technique in-
351 volves a large number of model evaluations (in our case, $10^6(n_p + 2)$, where n_p is the number
352 of model parameters), so we again utilized Gaussian process emulation. We calculated first
353 order Sobol' indices over a dense grid of time points to obtain a picture of how the sensitivity
354 changes over the time window of each experiment. While total sensitivity is often reported to
355 provide a complete picture of parameter sensitivity, we found that sensitivity to higher-order
356 parameter interactions was small for all experimental configurations. Hence, we limit our
357 analysis to first order indices.

358 Finally, we performed Bayesian calibration for each experimental configuration. In each
359 case, the model used for calibration is a Gaussian process emulator for the computationally-
360 expensive multi-physics code, and the likelihood function was derived using this model cou-

361 pled with an error model of independent and identically-distributed (iid) Gaussian noise.
362 For all three setups, we performed two Bayesian calibrations, each with the same data and
363 likelihood function but using two different prior distributions for the flow stress parameters.
364 First, we employed a bounded flat prior. All PTW parameters were assigned a truncated
365 uniform distribution (independent from all other parameters) reflecting the range of admis-
366 sible values. These bounds are given in Table 2. For our second prior, we used a collection of
367 truncated normal distributions for the PTW parameters. The truncated normal distributions
368 also used the same bounds as in the flat prior case. The mean and variance of the truncated
369 normal distributions for the flow stress parameters were chosen to reflect information from
370 a previous Bayesian calibration, which utilized the tantalum quasi-static, Kolsky bar, and
371 Taylor cylinder data referenced above. The truncated normal distributions implemented in
372 pyMC are such that they integrate to one. Priors pertaining to the non-PTW parameters
373 did not change over the two calibrations.

374 Note that sensitivity analysis is often used to down-select the set of calibrated paramete-
375 rs. Insensitive parameters can be fixed rather than estimated with minimal effect to the
376 calibration results. However, we opt to calibrate the full set of parameters in all cases, al-
377 lowing us to use the resulting Bayesian posteriors to validate the sensitivity analysis results.
378 In particular, the marginal posteriors for insensitive parameters will not be updated by the
379 data and will appear very similar to the marginal prior.

380 We now present the results of our uncertainty analysis. Each of the following subsections
381 pertains to a specific experimental configuration. In each subsection, we provide results of
382 Monte Carlo error propagation, sensitivity analysis, and Bayesian calibration.

383 5.1 Small Plate: LX-14 Results

384 The first experimental configuration is a small plate test with LX-14 pushing a tantalum
385 plate [3]. The tantalum strength model is a combination of the PTW for the flow stress and
386 the NP porosity model for the yield surface as described in 3.1.1 and 3.1.2, respectively. The
387 HE calibration parameters include the initial energy shift (denoted as E_{shift}), the freeze-out
388 pressure for reactions (P_{freeze}), and the charge thickness ($chrgthk$).

389 Monte Carlo Error Propagation

390 Figure 4 shows a comparison of the error propagation obtained with samples from the two dif-
391 ferent distributions. The response ensemble resulting from the bounded uniform distribution
392 exhibits a wider spread, which corresponds to larger output uncertainty. The uncertainty re-
393 sulting from the posterior draws is notably smaller with the spread of the responses visually
394 approaching a single curve.

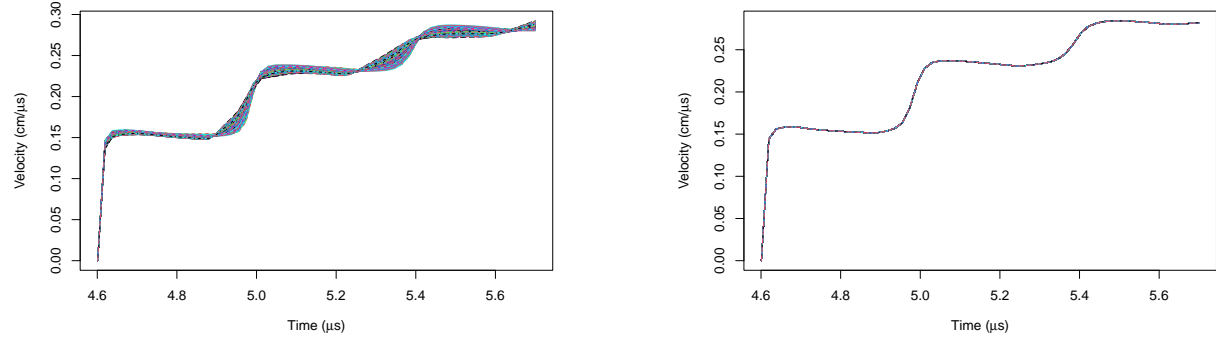


Figure 4: Monte Carlo error propagation for the small plate test with LX-14 with fixed HE and porosity parameters. Results are shown for (a) drawing PTW parameters from uniform distributions bounded by the ranges in Table 2 and (b) drawing PTW parameters from a narrower distribution (i.e., a posterior resulting from Bayesian calibration to focused strength experiments).

395 Sensitivity Analysis

396 Figure 5 visually presents the first order Sobol' indices as a function of time; the wider the
397 colored band, the more sensitive the corresponding parameter. Recall that the Sobol indices
398 partition the output variance to the variance of the parameters. Thus, the first order indices
399 sum to one if there is no sensitivity to higher-order parameter interactions (e.g., the joint
400 influence of two or more parameters).

401 For this experimental configuration, the HE parameter *shift* is obviously the most sensitive
402 parameter. Other parameters with a small but visually-observable level of sensitivity include
403 PTW parameters y_0 , $-\log(\gamma)$, κ , and s_0 . The HE charge thickness parameter is similarly
404 sensitive. The white dips into the plot near $5.0 \mu\text{s}$ and $5.4 \mu\text{s}$ indicate some sensitivity to
405 higher-order parameter interactions. In fact, of the three experimental configurations, the
406 LX-14 small plate model showed the highest sensitivity to multiple-parameter interactions.

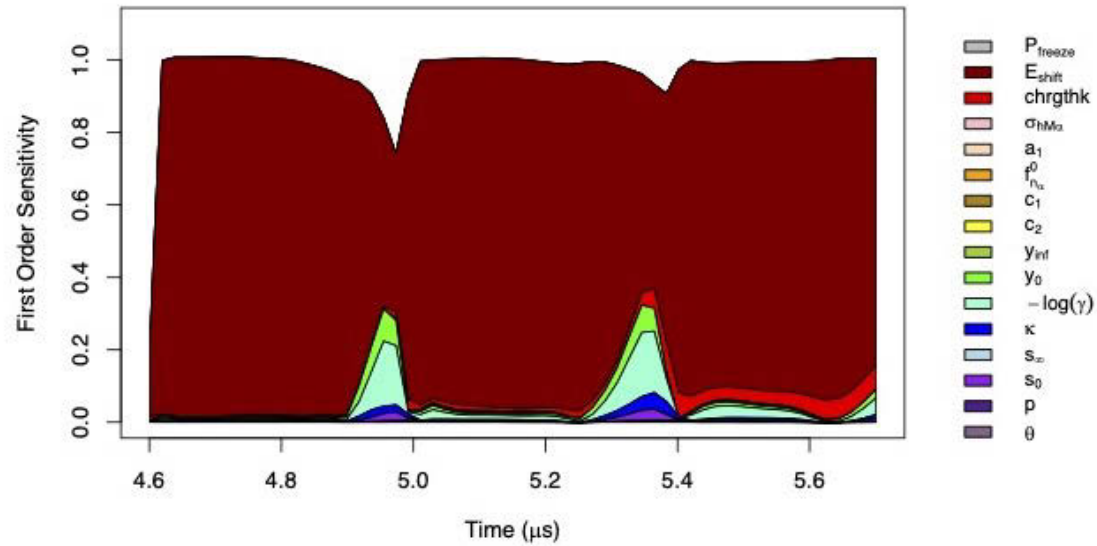


Figure 5: First order Sobol' indices for all parameters of the tantalum/LX-14 small plate test as a function of time.

407 Bayesian Inference

408 Recall that we are calibrating 16 parameters for the LX-14 small plate model: eight flow
 409 stress parameters and five porosity parameters as well as HE parameters E_{shift} , P_{freeze} , and
 410 charge thickness. We performed two Bayesian calibrations. First with a bounded flat prior
 411 for the PTW parameters and then with a truncated normal PTW prior. Priors for all
 412 other parameters were the same for both cases. With the exception of charge thickness, all
 413 parameters were assigned a truncated uniform prior (independent from all other parameters)
 414 reflecting the range of admissible values. Porosity parameter bounds are given in Table 3.
 415 For the HE parameters, the bounds were defined for the energy shift and the freeze pressure
 416 to provide adequate coverage of the experimental data. Since the charge thickness is a well-
 417 understood value recorded at the time of the experiment, we chose a truncated normal prior
 418 with the mean equal to the reported value and with truncation bounds given by $\pm 10\%$ of
 419 the nominal value to account for any potential measurement or transcription errors; this
 420 prior gives more weight to the recorded charge thickness as compared to a relatively non-
 421 informative flat prior.

422 We employed these two priors to determine if reducing the uncertainty in the flow stress
 423 parameters affects the inference of the other parameters. We now compare the results of the
 424 two calibrations. The resulting posteriors are plotted together in Figure 17. Due to the size
 425 of the plot, these results were placed in Appendix A. When calibration is performed with
 426 flat priors for the PTW parameters, the resulting marginal flow stress posteriors, with the

427 exception of those corresponding to κ and γ , remain relatively uninformed by the data—
 428 i.e., the posterior is very similar to the prior, which in this case is flat. This result agrees
 429 with the sensitivity analysis shown in Figure 5. Similar to the majority of the flow stress
 430 parameters, the marginal posteriors for NP porosity remain largely unchanged from their
 431 priors. For the HE parameters, E_{shift} —as expected from the sensitivity analysis—shows the
 432 greatest reduction in uncertainty when comparing the prior to the posterior. Calibration
 433 with the second prior results in narrower PTW marginal posteriors. This is expected since
 434 the truncated normal priors are more informative than the bounded flat priors. Note that
 435 the marginal posteriors of the non-PTW parameters appear to be unaffected by the change
 436 in the prior distribution. This suggests that prior knowledge about flow stress parameters
 437 does not aid in the inference of the HE and porosity parameters.

438 For a closer look at the HE parameter results, see Table 7 and Figure 6. In Table 7,
 439 we report for each HE parameter the *maximum a posteriori* (MAP) value as well as the
 440 posterior mean and standard deviation resulting from both calibrations. In Figure 6, we
 441 show plots comparing the HE parameter posteriors for both priors. As noted above, all HE
 442 parameter posteriors are largely unchanged by the different flow stress priors. This implies
 443 that for the tantalum/LX-14 small plate experiment, HE model parameter uncertainty is
 444 largely insensitive to metal strength and, thus, cannot be reduced by well-characterized flow
 445 stress parameters.

Table 7: LX-14 small plate parameter posterior MAP, mean, and standard deviation comparison

Parameter	MAP	Truncated Normal Mean (Std. Dev.)	Uniform Mean (Std. Dev.)
$chrghk$	3.891	3.890 (4.079e-2)	3.892 (3.895e-2)
E_{shift}	5.343e-3	5.766e-3 (1.780e-3)	5.886e-3 (1.789e-3)
P_{freeze}	2.000e4	9.722e+04 (5.046e4)	9.689e4 (5.027e4)

446 To characterize the uncertainty in the model response based on the posterior parameter
 447 uncertainty, we utilized Monte Carlo error propagation. 8000 posterior samples from the
 448 *truncated normal* calibration were propagated through the emulator to obtain an ensemble
 449 of predicted velocity curves. Note that 95% Bayesian credible intervals provide a more
 450 quantitative alternative to Monte Carlo error propagation. In both cases, the resulting
 451 uncertainty envelope does not reflect the uncertainty due to measurement noise and, thus,
 452 is not expected to cover the data (as would be the case if 95% prediction intervals were
 453 employed). With this in mind, we validate our calibrated model by plotting the ensemble of
 454 predicted velocities with the experimental data in Figure 7. Overall, the qualitative match
 455 to the data is good with a small excursion after the initial shock rise.

This is the author's peer reviewed, accepted manuscript. However, the online version of record will be different from this version once it has been copyedited and typeset.
PLEASE CITE THIS ARTICLE AS DOI: 10.1063/5.0226642

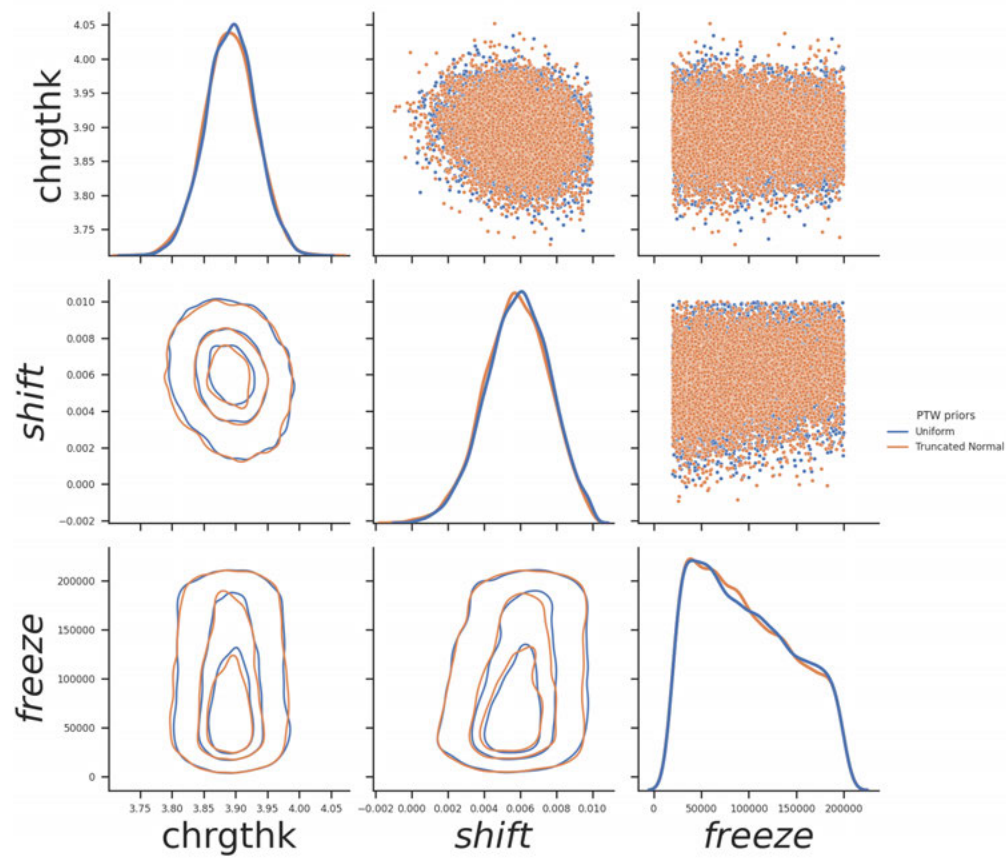


Figure 6: Tantalum/LX-14 small plate posterior comparison for the three HE parameters calibrated using Bayesian inference.

This is the author's peer reviewed, accepted manuscript. However, the online version of record will be different from this version once it has been copyedited and typeset.
PLEASE CITE THIS ARTICLE AS DOI: 10.1063/5.0226642

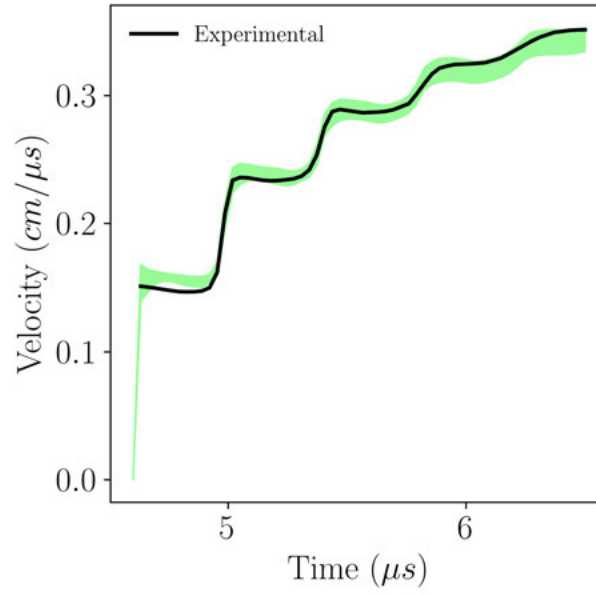


Figure 7: MC error propagation of the truncated normal posteriors and compared to the experimental data from Lee *et al.* [3] for the tantalum/LX-14 small plate test calibration. Here, the region in green is determined by the bounds of the velocity histories ensemble and the black line is the experimental data.

456 5.2 Small Plate: LX-17 Results

457 We again consider a small plate test but this time with LX-17 as the HE—that is, LX-17 is
458 used to push a thin tantalum plate [2]. For this configuration, we neglect porosity given that
459 results from previously-conducted analysis suggested that this configuration was insensitive
460 to such parameters. The PTW model is solely employed to characterize the metal's flow
461 strength. We also choose a different parameterization for the HE based on charge thickness
462 and soot. The latter is related to the soot produced during the detonation process and is
463 the molar volume used in the Murnaghan equation of state. This soot is an amorphous
464 solid comprised of carbon, nitrogen, and oxygen but not adhering to any specific molecular
465 structure. The change in HE model construction with the addition of amorphous soot is
466 reflective of recent soot recovery experiments and simulations.

467 Monte Carlo Error Propagation

468 A comparison of the resulting model response uncertainty from both error propagations
469 is shown in Figure 8. As with the previous experiment, the output uncertainty is greatly
470 reduced—almost vanishingly small—when the samples are drawn from the narrower, previously-
471 calibrated posterior.

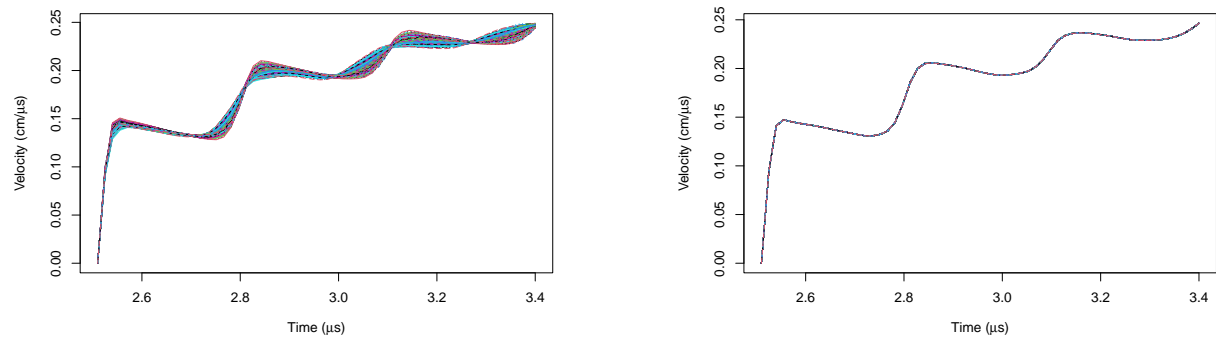


Figure 8: Monte Carlo error propagation for the small plate test with LX-17 with fixed HE and porosity parameters. Results are shown for (a) drawing PTW parameters from uniform distributions bounded by the ranges in Table 2 and (b) drawing PTW parameters from a narrower distribution (i.e., a posterior resulting from Bayesian calibration to focused strength experiments).

472 **Sensitivity Analysis**

473 As in Section 5.1, we obtain first order Sobol' indices—this time for the LX-17 small plate
474 model—as a function of time. The resulting Sobol' indices are plotted in Figure 9. The vast
475 majority of the sensitivity lies with the HE soot parameter. Other parameters showing a
476 discernible level of sensitivity include y_0 , $-\log(\gamma)$, and the charge thickness. Note that the
477 plot is nearly filled by the first order indices, indicating limited sensitivity due to parame-
478 ter interaction. The exception to this trend is the early time regime, which suggests that
479 parameter interaction may be influential before approximately $2.6 \mu\text{s}$.

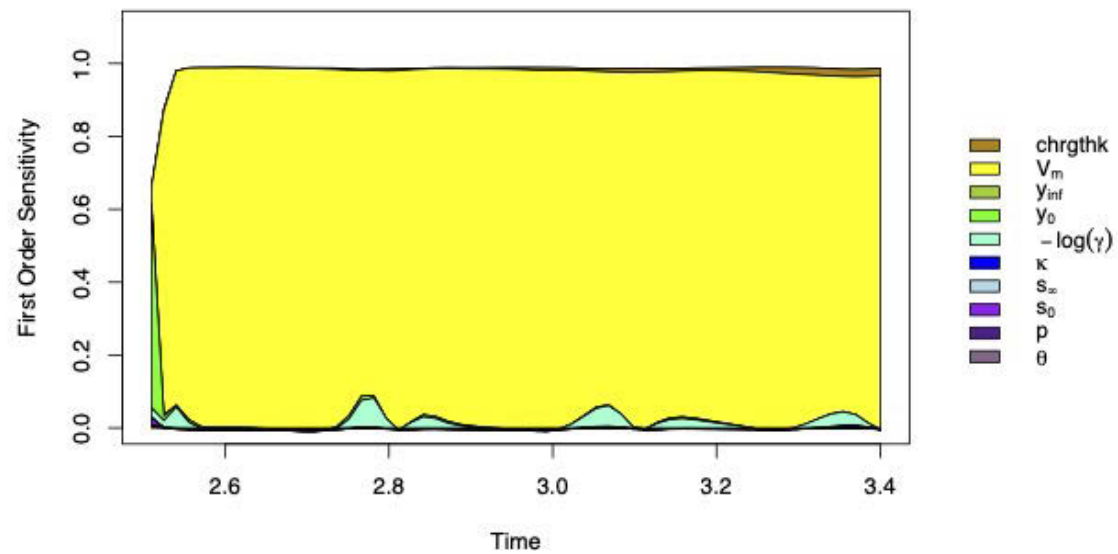


Figure 9: First order Sobol' indices for all parameters of the tantalum/LX-17 small plate test as a function of time.

480 **Bayesian Inference**

481 Ten parameters, including eight PTW parameters and HE parameters soot and charge thick-
482 ness, were used for calibration of our LX-17 small plate model. We compared calibration
483 results obtained with two different prior distributions: one with bounded uniform priors for
484 the PTW parameters and another with truncated normal priors for the PTW parameters.
485 In both cases, we chose a bounded uniform prior for the soot parameter and a truncated
486 normal prior for the charge thickness with the mean equal to the reported value and with
487 truncation bounds given by $\pm 10\%$ of the nominal value; the soot parameter bounds were
488 defined by the interval (4,8).

489 Utilizing these two priors allows us to explore the effect of better-characterized metal
490 strength parameters on the calibration of the HE parameters. In Table 8, the MAP, mean,
491 and standard deviations for both calibrations are reported for the soot parameter and the

Table 8: LX-17 small plate parameter posterior MAP, mean, and standard deviation comparison

Parameter	MAP	Truncated Normal Mean (Std. Dev.)	Uniform Mean (Std. Dev.)
V_m	5.996	5.992 (9.854e-2)	6.061 (1.045e-1)
$chrghk$	1.508	1.510 (5.626e-2)	1.470 (5.410e-2)

492 charge thickness. The informed priors for the metal correspond to a modest reduction in
493 uncertainty for the soot parameter, but the main point of interest is the effect of the shift in
494 the mean on the predicted velocity. The shift in the two posterior distributions is evident in
495 Figure 10. While visual inspection does not suggest a radical difference in these posteriors,
496 the HE modeling community considers a difference of 0.5% in the predicted velocity to
497 be *significant*. Thus, we compared hydrocode calculations for two sets of HE parameters,
498 corresponding to the posterior means from each choice of prior. The maximum velocities for
499 the for the difference in soot parameter means is 0.31% and for charge thickness means it
500 is 0.98%. This indicates that variations in charge thickness are something to consider and
501 include for historical experiments given the value reported will be an average of multiple
502 measurements on a nonuniform disk of HE.

503 As with the LX-14 small plate analysis, we characterized the model response uncertainty
504 by performing an Monte Carlo error propagation. This was done by densely sampling the
505 posteriors determined from the truncated normal PTW priors and propagating the resulting
506 parameter sets through the Gaussian process emulator. In Figure 11, the experimental data
507 is plotted with the shaded area corresponding to the spread of the model responses. Recall
508 from Section 5.1 that the propagated error envelope need not cover the data. Nevertheless,
509 we can validate the model by qualitatively assessing the goodness of fit to the data. Overall,
510 the model and data match well with some late-time deviations. This discrepancy could be
511 attributed to the 1-D assumptions used in the computational model being no longer valid as
512 2-D effects start to become dominate at late times.

513 5.3 Cylinder Test: LX-17 Results

514 Lastly, we analyze the most common experimental configuration for studying the detonation
515 velocity of HE materials. In the cylinder test configuration, a collection of HE pellets are
516 inserted into a metal cylinder and then detonated to expand the metal casing. Simulation
517 requires a 2-D axisymmetric computational model to accurately represent the experiment.
518 The specific HE/metal configuration modeled here is LX-17 pushing a tantalum cylinder
519 with the velocity being measured using Fabry-Perot laser interferometry. As with the other
520 experimental setups, we characterize tantalum flow stress with the PTW model. For porosity,
521 we employ the classical Gurson porosity model as described in Section 3.1.2.

This is the author's peer reviewed, accepted manuscript. However, the online version of record will be different from this version once it has been copyedited and typeset.
PLEASE CITE THIS ARTICLE AS DOI: 10.1063/5.0226642

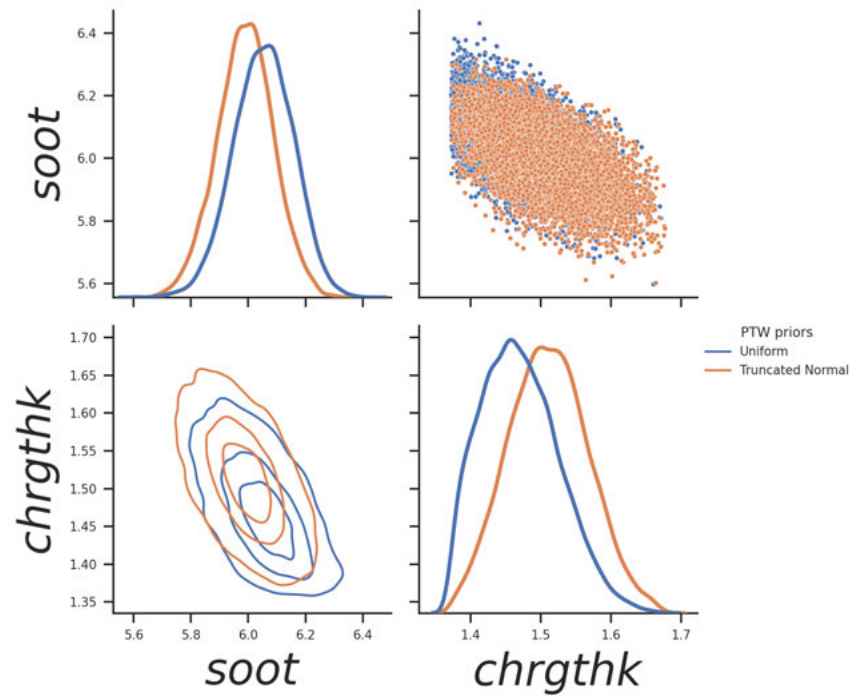


Figure 10: Comparison of the posteriors resulting from the uniform and truncated normal priors for *soot* and charge thickness.

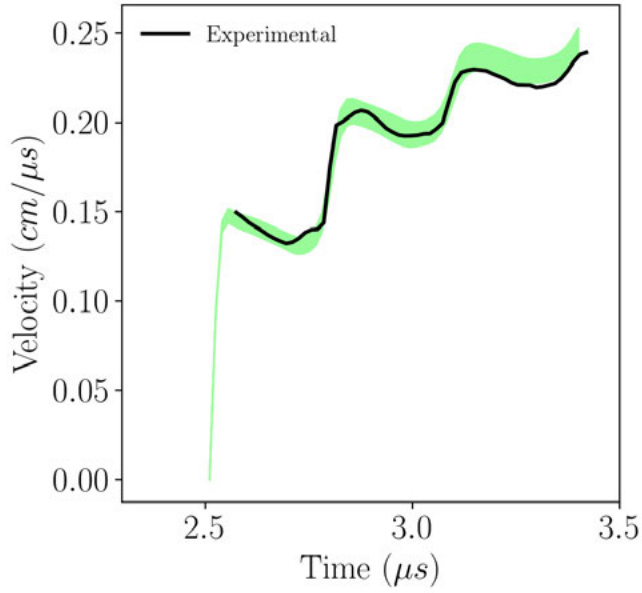


Figure 11: MC error propagation of the truncated normal posteriors and compared to the experimental data from Tarver *et al.* [2] for the LX-17/tantalum small plate test calibration.

522 Monte Carlo Error Propagation

523 As with the small plate experiments, we propagate Monte Carlo samples of the PTW pa-
 524 rameters from a bounded flat distribution and a previously-calibrated posterior. With all
 525 other parameters fixed, we obtain the response ensemble shown in Figure 12. Similarly to the
 526 other experimental configurations, drawing Monte Carlo samples out of a tighter distribution
 527 results in greater certainty with respect to the model response.

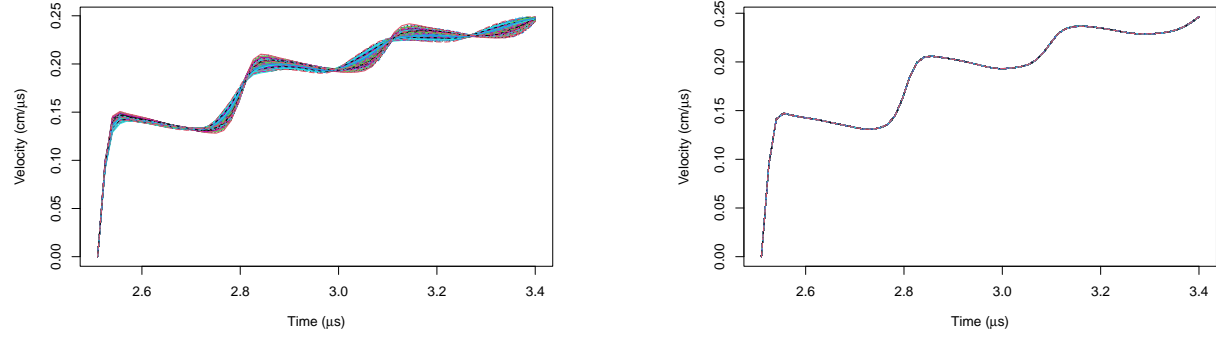


Figure 12: Monte Carlo error propagation for the cylinder test with LX-17 with fixed HE and porosity parameters. Results are shown for (a) drawing PTW parameters from uniform distributions bounded by the ranges in Table 2 and (b) drawing PTW parameters from a narrower distribution (i.e., a posterior resulting from Bayesian calibration to focused strength experiments).

528 Sensitivity Analysis

529 For our final sensitivity analysis, we calculate first order Sobol' indices for the LX-17 cylinder
 530 configuration. The Sobol' indices as a function of time are plotted in Figure 13. As with
 531 the previous experimental types, the sensitivity is dominated by an HE parameter. Here,
 532 E_{shift} is by far the most sensitive parameter. Other parameters with visually-discernible
 533 sensitivity include PTW parameters κ , $-\log(\gamma)$, and s_0 as well as porosity parameter q_2 and
 534 HE parameter P_{freeze} . Moreover, some sensitivity to higher-order interactions is indicated for
 535 the time window before approximately $39 \mu\text{s}$.

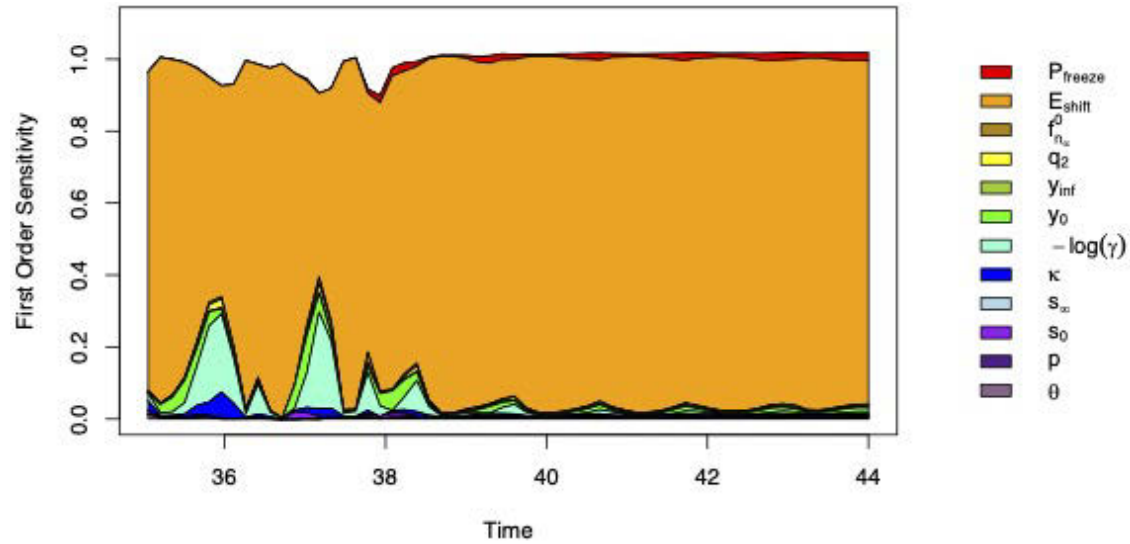


Figure 13: First order Sobol' indices for all parameters of the tantalum/LX-17 cylinder test as a function of time.

536 Bayesian Inference

537 Calibration of the LX-17 cylinder model involves 12 parameters: eight PTW parameters,
538 two porosity parameters, and two HE parameters. The HE model used in this calibration is
539 the same as the one used for the LX-14 configuration, employing energy density shift and
540 chemical-freeze-out pressure parameters. We again carried out two calibrations, which em-
541 ploy priors encoding differing levels of information about the PTW parameters—specifically,
542 a non-informative bounded uniform prior and a more-informed truncated normal prior. In
543 both cases, the non-flow stress parameters were assigned bounded uniform priors. (See
544 Tables 3 and 5 for bounds).

545 We compare the resulting posteriors of the two calibrations to ascertain how knowledge
546 of the metal strength can influence the posteriors of other parameters. Table 9 provides a
547 summary of the calibration for the HE and porosity parameters. Figures 14 and 15 show an
548 overlay of both posteriors for the HE and porosity models, respectively. Of all of the con-
549 figurations, the non-flow stress parameters of the LX-17 cylinder model showed the greatest
550 sensitivity to the different PTW parameter priors. Modest differences are present in the HE
551 posterior comparison with the posteriors from the more informative priors showing a slight
552 reduction in uncertainty, but a notable effect is displayed with the porosity posteriors. Figure
553 15 shows a significant narrowing of the porosity model posteriors when a more informative
554 prior is used for the PTW parameters. This suggests that incorporating flow-stress-related
555 knowledge results in better-constrained porosity parameters.

556 Note the narrowing of the q_2 parameter, which controls the porosity evolution. Given

557 that ductile failure of metals is related to the complexity of the loading condition and that
 558 the cylinder test will evolve non-uniform deformation as well as transients in strain rate,
 559 pressure, and temperature due to the complexity of HE loading, it is valuable to constrain
 560 porosity-related parameters for applications that extrapolate beyond the subset of focused
 561 experiments in this study.

Table 9: LX-17 cylinder test parameter posterior MAP, mean, and standard deviation comparison

Parameter	MAP	Truncated Normal Mean (Std. Dev.)	Uniform Mean (Std. Dev.)
q_2	0.798	0.747 (9.467e-2)	0.752 (1.425e-1)
f_{T_σ}	5.999	4.648 (1.012)	3.967 (1.156)
E_{shift}	-1.14e-4	-1.348e-04 (1.164e-3)	2.442e-4 (1.256e-3)
P_{freeze}	9.681e4	9.197e4 (2.098e4)	8.947e4 (2.151e4)

562 In addition to the truncated normal priors for the PTW model, we include *informed* priors
 563 for the Gurson porosity model parameters with the mean being the average of uniform bounds
 564 and the standard deviation set to $\pm 10\%$ of the mean. This more informative prior will help
 565 us determine if a well-calibrated porosity model could further reduce the uncertainty of the
 566 HE parameters. Given the strong dependence on the global response of E_{shift} and P_{freeze}
 567 parameters, it is unsurprising that for a model calibration a tighter porosity prior results in
 568 a negligible difference in the HE posteriors.

569 As with the small plate configurations, Monte Carlo error propagation was used to study
 570 the effect of the parameter uncertainty on the model response uncertainty. We sampled pa-
 571 rameter sets from the *informed porosity* posterior and propagated them through the Gaussian
 572 process emulator. Figure shows the spread of the resulting response ensemble plotted with
 573 the experimental data. Visual inspection suggests that the model provides a good fit to the
 574 experimental data.

575 Lastly, the posterior means and standard deviations. for the PTW parameters for all
 576 three configurations can be found in Appendix A, in Figures 17, 18, and 19, and compared
 577 to those used in the truncated normal priors in Tables 10, 11, and 12. Notably, while there
 578 is some shifts and reduction in standard deviations there the differences are relatively small.

579 5.4 Additional Discussion of Interaction and Ambiguity in the 580 Joint Inference of Metal and HE parameters

581 An intriguing observation of the present work is that certain HE parameters (specifically
 582 P_{freeze} and E_{shift}) may be strongly, and nearly unambiguously, inferred from the small plate
 583 and cylinder tests. Even in the presence of sizable strength and porosity uncertainty, these
 584 may successfully be inferred. In contrast, other parameters such as the soot parameter, V_m ,

This is the author's peer reviewed, accepted manuscript. However, the online version of record will be different from this version once it has been copyedited and typeset.
PLEASE CITE THIS ARTICLE AS DOI: 10.1063/1.50226642

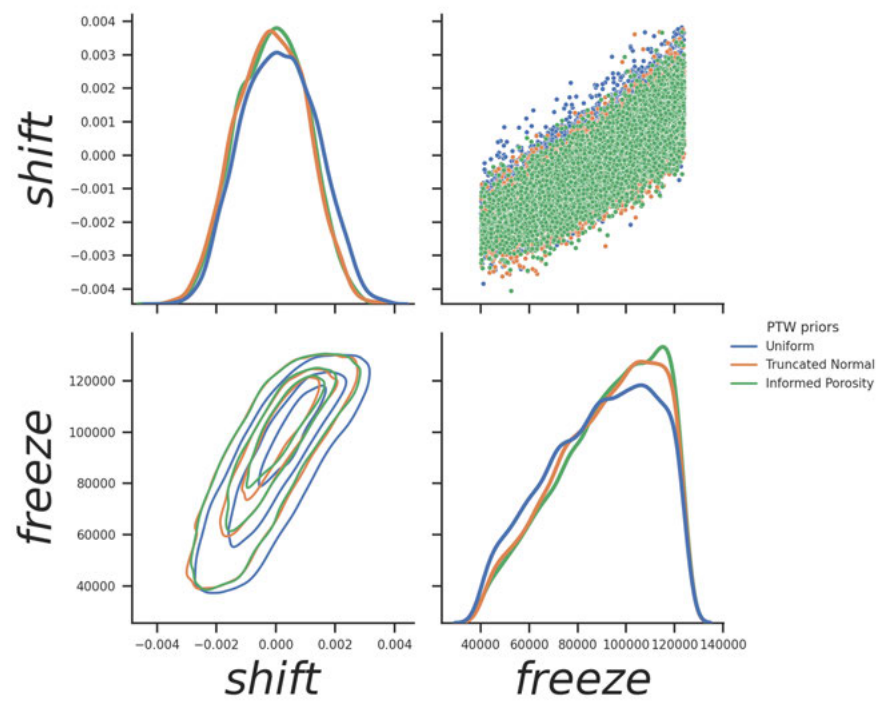


Figure 14: HE parameter posteriors for LX-17 calibration for the cylinder test configuration.

This is the author's peer reviewed, accepted manuscript. However, the online version of record will be different from this version once it has been copyedited and typeset.
PLEASE CITE THIS ARTICLE AS DOI: 10.1063/5.0226642

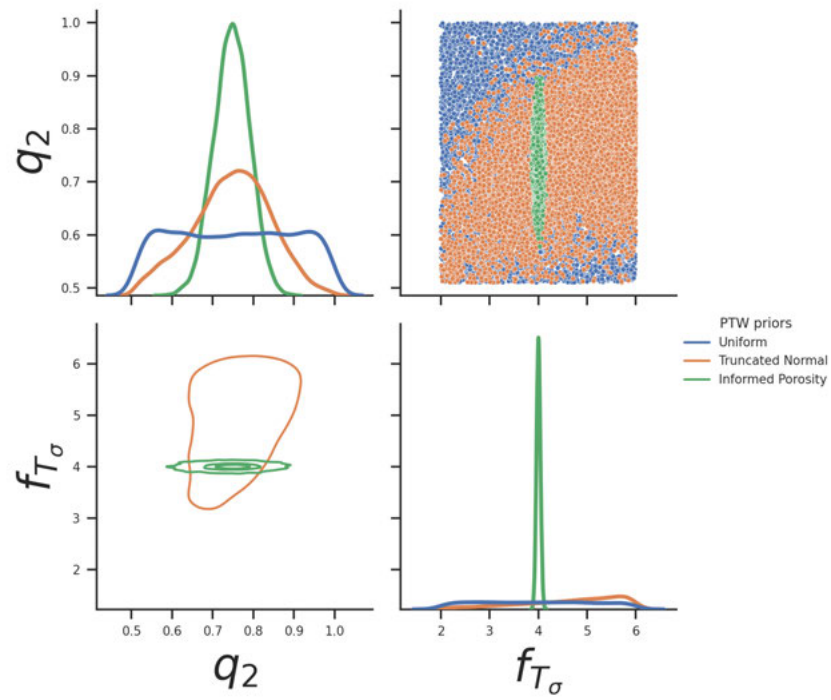


Figure 15: Porosity model posterior comparison for the Gurson model used in the LX-17 cylinder test calibration.

This is the author's peer reviewed, accepted manuscript. However, the online version of record will be different from this version once it has been copyedited and typeset.
PLEASE CITE THIS ARTICLE AS DOI: 10.1063/5.0226642

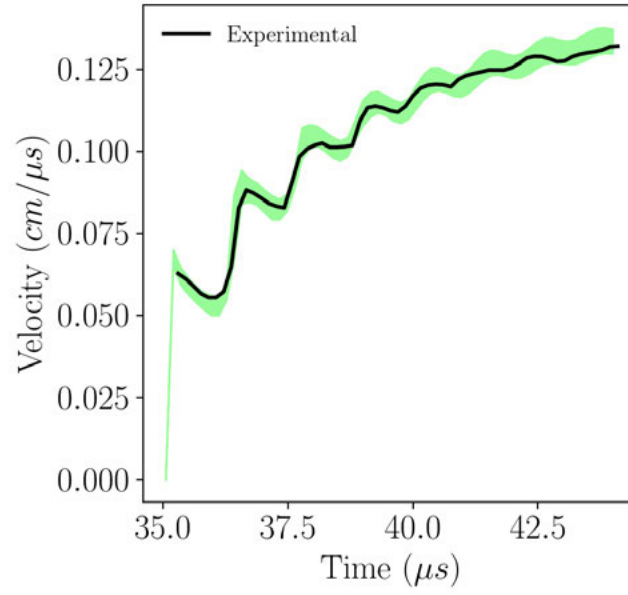


Figure 16: MC error propagation of the informed porosity posteriors and compared to the experimental data from Aldis *et al.* [1] for the tantalum/LX-17 cylinder test calibration. Here, the region in green is determined by the bounds of the velocity histories ensemble and the black line is the experimental data.

585 exhibit strong dependence on aspects of the metal physical behavior and specifically the
586 prior utilized for the PTW model parameters. This leads us to question why this difference
587 exists and if we can learn something more general about parameter interactions within many
588 the choices of physics models.

589 We conjecture that the parameters that have to do specifically with the energy density
590 of the high explosive may be nearly unambiguously inferred in these small-scale science
591 experiments whereas others (having to do with rate of energy release or specific properties
592 of the reaction products) may be closely coupled to the behavior of the metal strength and
593 porosity. To understand this, it is useful to consider the classical Gurney equation for an
594 cylindrical charge:

$$\frac{V}{\sqrt{2E}} = \left(\frac{M}{C} + \frac{1}{2} \right)^{-1/2},$$

595 where V and M are the velocity and mass of the metal and E and C are the energy and
596 the mass of the high explosive, respectively. This equation is a coarse estimate utilizing
597 only conservation of energy and some simple kinematic assumptions. However, even if it
598 is not exact, it suggests a one-to-one dependence of the asymptotic velocity on the initial
599 energy density of the high explosive. Thus, one might reason that parameters characterizing
600 the energy of the high explosive such as P_{freeze} and E_{shift} to be strongly constrained by any
601 experimental measurement, including the asymptotic velocity, simply as a consequence of
602 energy conservation. On the other hand, the *specific details* of the energy release including
603 timing and specific behaviors of the products such as is characterized by the V_m parameter
604 are not a priori constrained in a such a direct way. In these instances, we therefore expect
605 that *simultaneous* inference of the inelastic behavior of the metal and the HE parameters to
606 be a critical aspect of learning about the behavior of energetic materials.

607 6 Conclusion

608 This article has presented a Bayesian analysis of high explosive-driven experiments, includ-
609 ing plate and cylinder experiments of both LX-14 and LX-17. The goal of this work was to
610 simultaneously assess the inelastic behavior of metals and the behavior of materials simulta-
611 neously from metal/HE experiments. We estimated the optimal parameters of Cheetah-based
612 reactive-flow models of the energetic materials, the plasticity behavior, and the porosity be-
613 havior simultaneously. We used a relatively simple model for tantalum, the specific metal
614 under consideration. Utilizing constraints from focused metal experiments, we were able to
615 assess the effects of uncertainty in the metal material model on the metal/HE experiments.
616 Note that the specific quantitative results described here for tantalum may not transfer to the
617 use of other metals, such as copper, in coupled metal/HE experiments, but the methodology
618 applied here is transferable to other HE/metal system.

619 Intriguingly, for our tantalum/HE models, significantly reducing uncertainty in the metal

620 prior has *minimal* effect on the HE model parameters pertaining to the energy content of the
621 material; however, there is a *significant* effect on other HE model parameters such as molar
622 density of soot formed through detonation, V_m . Some energetic material parameters—such
623 as E_{shift} and P_{freeze} , which are associated with the basic energy content of the HE—are
624 strongly constrained by the experimental data and are relatively insensitive to the priors
625 of the plasticity model. In contrast, inference of the soot density and charge thickness are
626 sensitive to the choice of prior for the plasticity models. Analysis of the velocimetry is
627 suggestive that the charge thickness appears to have small effect on the velocity prediction
628 up to 0.9%. This implies that we may safely utilize historical HE data (with possibly high
629 uncertainty in the reported charge thickness), but given the specificity of the models, data
630 sets, etc. considered in our study, this should not be taken as absolute.

631 Based on our results, we offer recommendations for future statistical analysis and ex-
632 perimentation. When performing statistical inference, it would be beneficial to estimate
633 charge dimensions when calibrating to historical data. Additionally, HE model parameters
634 may benefit from relatively basic metal strength characterization when performing coupled
635 metal/HE experiments for model calibration. Furthermore, we have observed some interest-
636 ing interactions between the plasticity and the porosity model; prior knowledge of metal flow
637 stress model parameters allows for improved calibration of metal porosity model parameters
638 in cylinder tests. Hence, performing experiments with well-characterized metal is suggested.
639 Next, the small plate calibration potentially indicates that insensitive HEs may exhibit more
640 sensitivity to metal strength than conventional HEs. This indicates that when performing
641 experiments with insensitive HEs it is especially important to use a well-characterized metal.

642 Lastly, HE lot to lot variability not considered in this study. We close this study by offer-
643 ing some suggestions for future work in this area. First, we suspect that the decomposition
644 of HE parameters into two classes—those having to do with the HE energy content and those
645 which have to do with specific details of the products—may suggest future experiments and
646 methods of analysis by which to learn about HEs; an obvious extension would be to explore
647 the uncertainty related to HE density variations that are known to exist. Additionally, us-
648 ing a statistically-motivated design of experiments strategy, additional experiments could be
649 designed to maximize the information gained about parameters that are more challenging
650 to define unambiguously when including the uncertainty arising from the metal. Second, we
651 suggest that further work is needed to specifically examine the interplay between plasticity
652 and porosity models; the correlations arising in our results among these parameters are con-
653 sistent with the physics of the strength models. It will be important to utilize experiments
654 in future analyses that are insensitive to the plasticity-porosity interaction, helping to dis-
655 ambiguate the causal behaviors. Finally, we endorse that analysis of model form error in
656 the HE model as a valuable direction of inquiry and would likely have a profound impact on
657 understanding uncertainty.

This is the author's peer reviewed, accepted manuscript. However, the online version of record will be different from this version once it has been copyedited and typeset.
PLEASE CITE THIS ARTICLE AS DOI: 10.1063/5.0226642

658 **Acknowledgments**

659 This work is performed under the auspices of the U.S. Department of Energy by Lawrence
660 Livermore National Laboratory under Contract DEAC52-07NA27344 (LLNL-JRNL-864794).

This is the author's peer reviewed, accepted manuscript. However, the online version of record will be different from this version once it has been copyedited and typeset.
PLEASE CITE THIS ARTICLE AS DOI: 10.1063/5.0226642

661 Appendix

662 A Full Posteriors

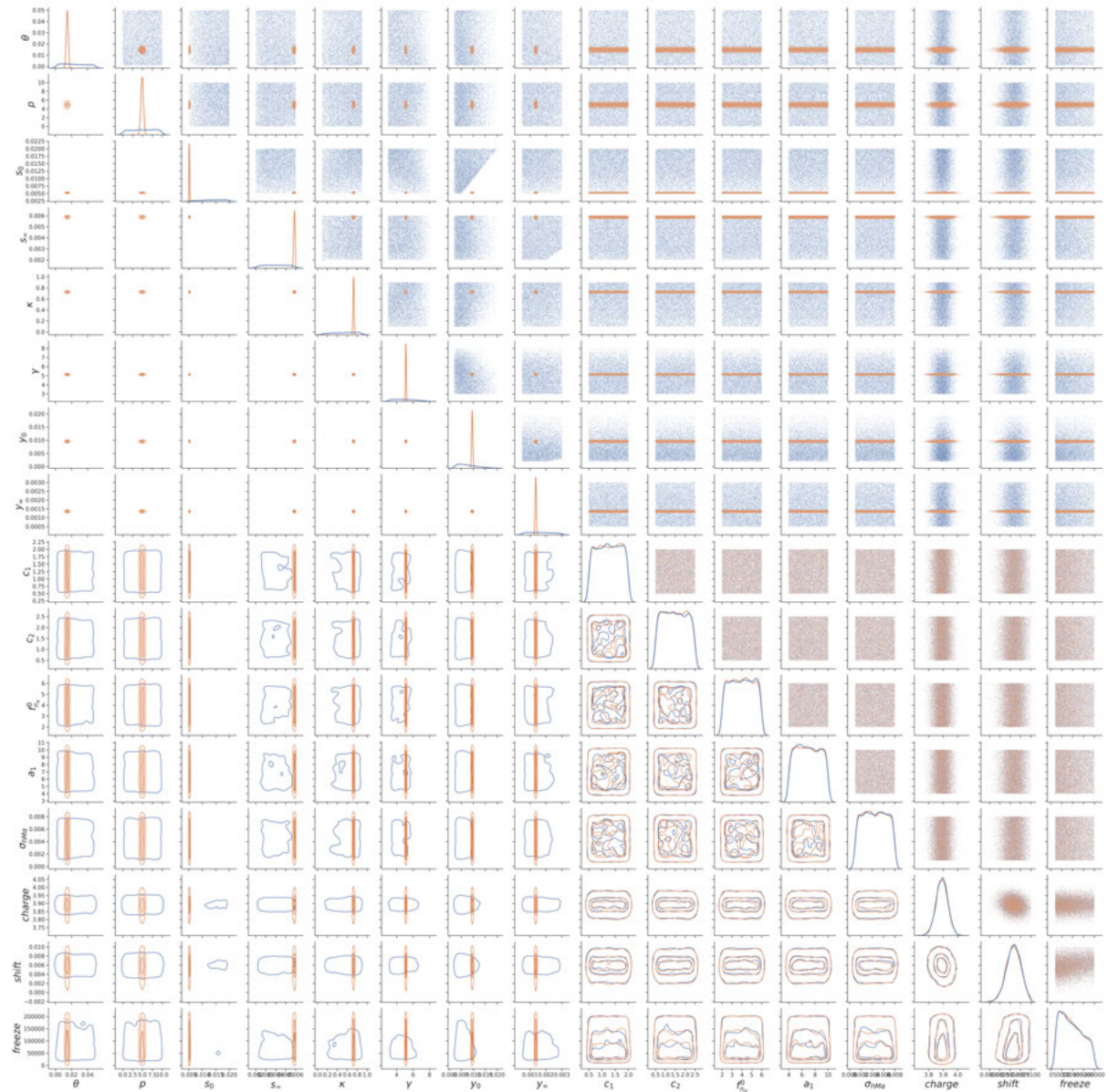


Figure 17: Complete Parameter posterior comparison for the LX-14 small plate configuration

This is the author's peer reviewed, accepted manuscript. However, the online version of record will be different from this version once it has been copyedited and typeset.
PLEASE CITE THIS ARTICLE AS DOI: 10.1063/1.50226642

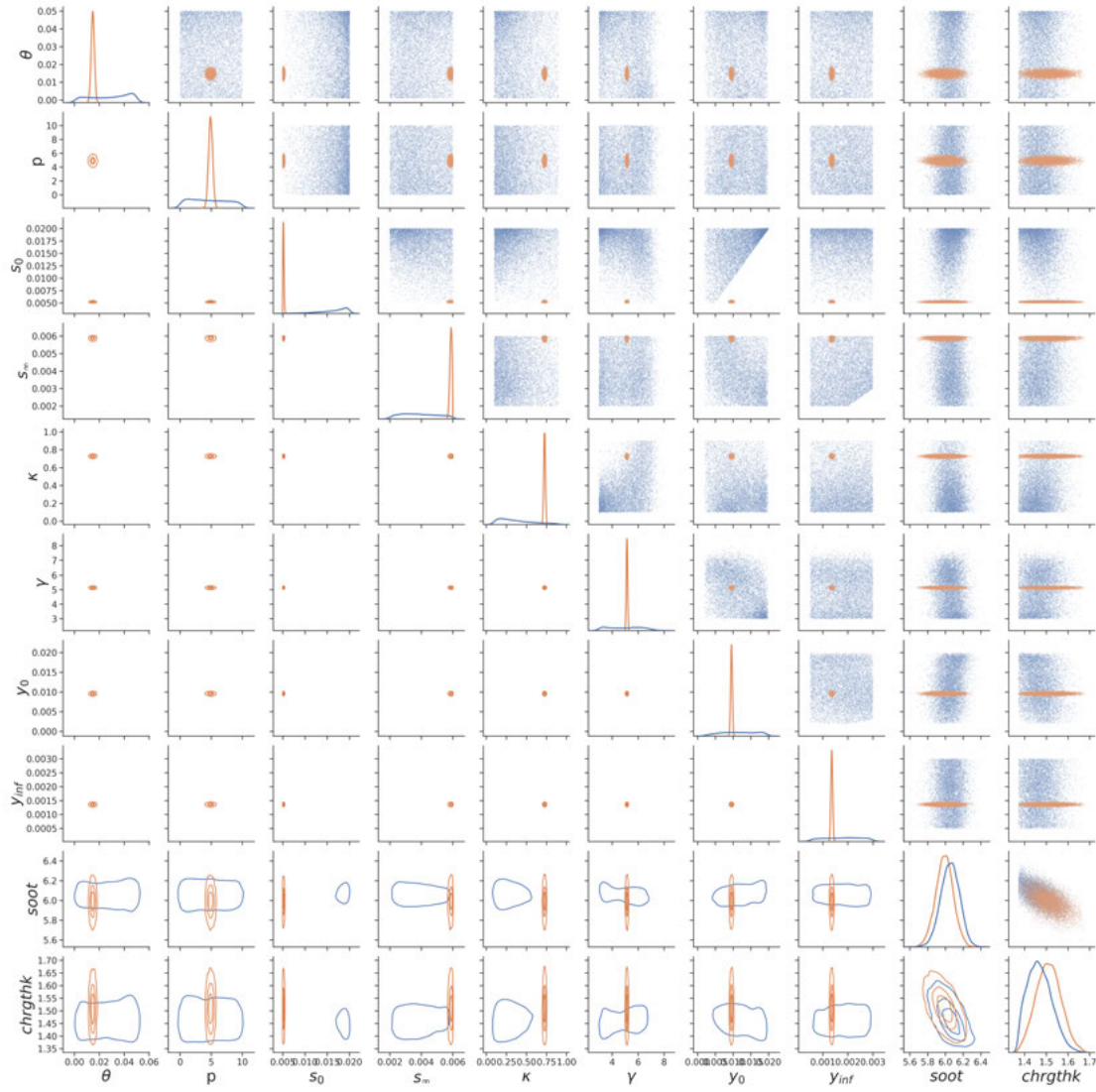


Figure 18: Complete Parameter posterior comparison for the LX-17 small plate configuration

This is the author's peer reviewed, accepted manuscript. However, the online version of record will be different from this version once it has been copyedited and typeset.
PLEASE CITE THIS ARTICLE AS DOI: 10.1063/5.0226642

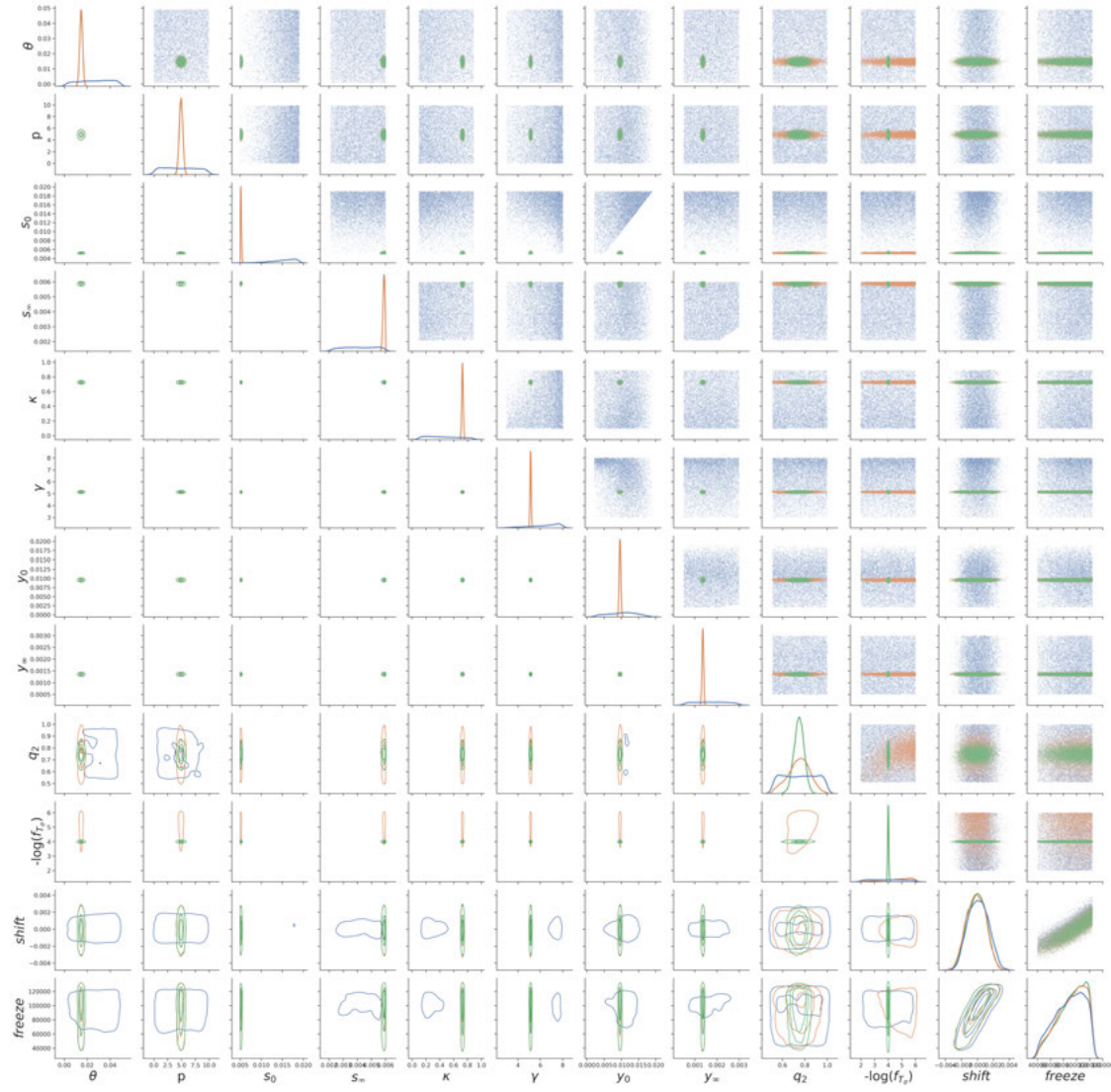


Figure 19: Complete parameter posterior comparison for the LX-17 cylinder test configuration

Table 10: PTW model parameters with a comparison of calibrations for smplt-lx-14 and those used in the truncated normal prior distributions.

Parameter	smplt-LX14	Truncated normal mean (Std. Dev.)	Units
θ	0.0242($1.440 \cdot 10^{-02}$)	0.0148($1.878 \cdot 10^{-06}$)	-
p	5.106 (2.891)	4.913 (0.3143)	-
s_0	0.0136($3.979 \cdot 10^{-03}$)	0.006316($1.235 \cdot 10^{-04}$)	-
s_∞	0.00403($5.877 \cdot 10^{-03}$)	0.00588($6.84 \cdot 10^{-05}$)	-
κ	0.533 ($1.435 \cdot 10^(-03)$)	0.727 ($1.014 \cdot 10^(-02)$)	-
γ	$-\log(10^{5.022})(-\log(10^{1.225}))$	$-\log(10^{5.134})(-\log(10^{0.00497}))$	-
y_0	0.00753($3.828 \cdot 10^{-03}$)	0.00629($1.241 \cdot 10^{-04}$)	-
y_∞	0.001671($7.017 \cdot 10^{-04}$)	0.00136($3.626 \cdot 10^{-05}$)	-

Table 11: PTW model parameters with a comparison of calibrations for smplt-lx-17 and those used in the truncated normal prior distributions.

Parameter	smplt-lx17	Truncated normal mean (Std. Dev)	Units
θ	0.0282($1.53 \cdot 10^{-02}$)	0.0148($1.260 \cdot 10^{-03}$)	-
p	4.672 (2.882)	4.916 (0.3159)	-
s_0	0.01623($6.317 \cdot 10^{-03}$)	0.00632($1.229 \cdot 10^{-04}$)	-
s_∞	0.003927($1.112 \cdot 10^{-03}$)	0.00588($6.72 \cdot 10^{-05}$)	-
κ	0.368 (0.203)	0.727 (0.0104)	-
γ	$-\log(10^{4.987})(-\log(10^{1.231}))$	$-\log(10^{5.138})(-\log(10^{0.0518}))$	-
y_0	0.01160($4.690 \cdot 10^{-03}$)	0.006299($1.235 \cdot 10^{-04}$)	-
y_∞	0.001780($7.051 \cdot 10^{-04}$)	0.00136($3.617 \cdot 10^{-05}$)	-

Table 12: PTW model parameters with a comparison of calibrations for cyl-lx-17 and those used in the truncated normal prior distributions.

Parameter	cyl-LX17	Truncated normal mean (Std. dev)	Units
θ	0.0267($1.484 \cdot 10^{-02}$)	0.0148($1.258 \cdot 10^{-03}$)	-
p	4.807 (2.847)	4.904 (0.3280)	-
s_0	0.01509($2.9712 \cdot 10^{-03}$)	0.00632($1.227 \cdot 10^{-04}$)	-
s_∞	0.004134($1.098 \cdot 10^{-03}$)	0.00588($6.79 \cdot 10^{-05}$)	-
κ	0.754(0.225)	0.727 (0.0105)	-
γ	$-\log(10^{5.134})(-\log(10^{0.00258}))$	$-\log(10^{5.132})(-\log(10^{0.00259}))$	-
y_0	0.01014($3.979 \cdot 10^{-03}$)	0.00631($1.235 \cdot 10^{-04}$)	-
y_∞	0.00172($1.360 \cdot 10^{-03}$)	0.00136($3.653 \cdot 10^{-05}$)	-

663 **References**

- 664 [1] D F Aldis, W Quirk, and R D Breithaupt. The effect of detonation curvature on
665 cylindrical wall motion. *UCRL-ID-107480*, 1991.
- 666 [2] Craig M. Tarver, John W. Kury, and R. Don Breithaupt. Detonation waves in tri-
667 aminotrinitrobenzene. *Journal of Applied Physics*, 82(8):3771–3782, 10 1997.
- 668 [3] E Lee, D Breithaupt, C McMillan, N Parker, J Kury, C Tarver, W Quirk, and J Walton.
669 Motion of thin metal walls and the equation of state of detonation products. [lx-14 con-
670 taining 95% hmx and 5% polyurethane]. *8th Symposium (International) on Detonation*,
671 page 613, 1985.
- 672 [4] N. R. Barton and M. Rhee. A multiscale strength model for tantalum over an extended
673 range of strain rates. *Journal of Applied Physics*, 114(12):123507, 2013.
- 674 [5] Michael B. Prime, Athanasios Arsenlis, Ryan A. Austin, Nathan R. Barton, Corbett C.
675 Battaile, Justin L. Brown, Leonid Burakovsky, William T. Buttler, Shuh-Rong Chen,
676 Dana M. Dattelbaum, Saryu J. Fensin, Dawn G. Flicker, George T. Gray, Carl Greeff,
677 David R. Jones, J. Matthew D. Lane, Hojun Lim, D.J. Luscher, Thomas R. Mattsson,
678 James M. McNaney, Hye-Sook Park, Philip D. Powell, Shon T. Prsbrey, Bruce A.
679 Remington, Robert E. Rudd, Sky K. Sjue, and Damian C. Swift. A broad study of
680 tantalum strength from ambient to extreme conditions. *Acta Materialia*, page 117875,
681 2022.
- 682 [6] Matthew Nelms, Jonathan Lind, Jonathan Margraf, Sayyad Basim Qamar, Joshua Her-
683 rington, Andrew Robinson, Mukul Kumar, and Nathan Barton. High-rate strength re-
684 sponse of tantalum from dynamic hole closure experiments. *Journal of Applied Physics*,
685 132(17), 11 2022. 175102.
- 686 [7] WJ Schill, RA Austin, KL Schimdt, JL Brown, and NR Barton. Simultaneous inference
687 of the compressibility and inelastic response of tantalum under extreme loading. *Journal*
688 *of Applied Physics*, 130(5):055901, 2021.
- 689 [8] W Schill, R Austin, J Brown, and N Barton. anelasticity and phase transition during
690 ramp-release in tin. *Journal of Dynamic Behavior of Materials*, 7(2):207–216, 2021.
- 691 [9] Nathan Barton, Ryan Austin, Justin Brown, and Moono Rhee. Anelastic effects on
692 reverse loading–connection to evolving dislocation structure. *Bulletin of the American*
693 *Physical Society*, 64, 2019.
- 694 [10] J. N. Johnson, R. S. Hixson, D. L. Tonks, and G. T. Gray III. Shock compression and
695 quasielastic release in tantalum. In S. C. Schmidt, J. W. Shaner, G. A. Samara, and

- 696 M. Ross, editors, *High-pressure science and technology*, volume 309 of *AIP conference*
697 *proceedings*, pages 1095–1098. AIP Press, 1994.
- 698 [11] J. M. Winey, J. N. Johnson, and Y. M. Gupta. Unloading and reloading response
699 of shocked aluminum single crystals: Time-dependent anisotropic material description.
700 *Journal of Applied Physics*, 112(9):093509, 2012.
- 701 [12] J. L. Brown, C. S. Alexander, J. R. Asay, T. J. Vogler, and J. L. Ding. Extracting
702 strength from high pressure ramp-release experiments. *Journal of Applied Physics*,
703 114(22):223518, 2013.
- 704 [13] Bryan W Reed, James S Stolken, Roger W Minich, and Mukul Kumar. A uni-
705 fied approach for extracting strength information from nonsimple compression waves.
706 part i: Thermodynamics and numerical implementation. *Journal of Applied Physics*,
707 110(11):113505, 2011.
- 708 [14] SJ Ali, RG Kraus, DE Fratanduono, DC Swift, and JH Eggert. An iterative forward
709 analysis technique to determine the equation of state of dynamically compressed mate-
710 rials. *Journal of Applied Physics*, 121(19):195901, 2017.
- 711 [15] S. J. Ali, D. C. Swift, C. J. Wu, and R. G. Kraus. Development of uncertainty-aware
712 equation-of-state models: Application to copper. *Journal of Applied Physics*, 128(18),
713 11 2020. 185902.
- 714 [16] J. L. Brown and L. B. Hund. Estimating material properties under extreme conditions
715 by using bayesian model calibration with functional outputs. *Journal of the Royal*
716 *Statistical Society: Series C (Applied Statistics)*, 67(4):1023–1045, 2018.
- 717 [17] Jason Bernstein, Kathleen Schmidt, David Rivera, Nathan Barton, Jeffrey Florando,
718 and Ana Kupresanin. A comparison of material flow strength models using bayesian
719 cross-validation. *Computational Materials Science*, 169:109098, 2019.
- 720 [18] David J Walters, Ayan Biswas, Earl C Lawrence, Devin C Francom, Darby J Luscher,
721 D Anthony Fredenburg, Kelly R Moran, Christine M Sweeney, Richard L Sandberg,
722 James P Ahrens, et al. Bayesian calibration of strength parameters using hydrocode
723 simulations of symmetric impact shock experiments of al-5083. *Journal of Applied*
724 *Physics*, 124(20):205105, 2018.
- 725 [19] Ralph C. Smith. *Uncertainty Quantification: Theory, Implementation, and Applica-*
726 *tions*. Number 12 in Computational Science and Engineering. SIAM, 2013.
- 727 [20] Andrew Gelman, Hal S Stern, John B Carlin, David B Dunson, Aki Vehtari, and Don-
728 ald B Rubin. *Bayesian data analysis*. Chapman and Hall/CRC, 2013.

- 729 [21] Jim A Gaffney, Dan Clark, Vijay Sonnad, and Stephen B Libby. Development of a
730 bayesian method for the analysis of inertial confinement fusion experiments on the nif.
731 *Nuclear Fusion*, 53(7):073032, 2013.
- 732 [22] JJ Ruby, JR Rygg, DA Chin, JA Gaffney, PJ Adrian, D Bishel, CJ Forrest, V Yu Gle-
733 bov, NV Kabadi, PM Nilson, et al. Constraining physical models at gigabar pressures.
734 *Physical Review E*, 102(5):053210, 2020.
- 735 [23] Jim A Gaffney, Scott T Brandon, Kelli D Humbird, Michael KG Kruse, Ryan C Nora,
736 J Luc Peterson, and Brian K Spears. Making inertial confinement fusion models more
737 predictive. *Physics of Plasmas*, 26(8):082704, 2019.
- 738 [24] PF Knapp, WE Lewis, VR Joseph, CA Jennings, and ME Glinsky. Optimizing the
739 configuration of plasma radiation detectors in the presence of uncertain instrument
740 response and inadequate physics. *Journal of Plasma Physics*, 89(1):895890101, 2023.
- 741 [25] JJ Ruby, JA Gaffney, JR Rygg, Y Ping, and GW Collins. High-energy-density-physics
742 measurements in implosions using bayesian inference. *Physics of Plasmas*, 28(3):032703,
743 2021.
- 744 [26] MF Kasim, TP Galligan, Jacob Topp-Mugglestone, Gianluca Gregori, and SM Vinko.
745 Inverse problem instabilities in large-scale modeling of matter in extreme conditions.
746 *Physics of Plasmas*, 26(11):112706, 2019.
- 747 [27] Udo Von Toussaint. Bayesian inference in physics. *Reviews of Modern Physics*,
748 83(3):943, 2011.
- 749 [28] Thao Nguyen, Devin C Francom, Darby Jon Luscher, and JW Wilkerson. Bayesian
750 calibration of a physics-based crystal plasticity and damage model. *Journal of the*
751 *Mechanics and Physics of Solids*, 149:104284, 2021.
- 752 [29] Juan L de Pablos, Ilchat Sabirov, and Ignacio Romero. An experimental, computational,
753 and statistical strategy for the bayesian calibration of complex material models. *Archives*
754 *of Computational Methods in Engineering*, pages 1–30, 2023.
- 755 [30] Devin Francom, Bruno Sansó, Ana Kupresanin, and Gardar Johannesson. Sensitivity
756 analysis and emulation for functional data using Bayesian adaptive splines. *Statistica*
757 *Sinica*, 28:791–816, 2018.
- 758 [31] Kathleen Schmidt, Jason Bernstein, Nathan Barton, Jeffrey Florando, and Ana Kupre-
759 sanin. Sensitivity analysis of strength models using Bayesian adaptive splines. In *AIP*
760 *Conference Proceedings*, volume 1979, page 140004. AIP Publishing LLC, 2018.

- 761 [32] Dave Higdon, James Gattiker, Brian Williams, and Maria Rightley. Computer model
762 calibration using high-dimensional output. *Journal of the American Statistical Association*,
763 103(482):570–583, 2008.
- 764 [33] Kibaek Lee, Alberto M. Hernández, D. Scott Stewart, and Seungjoon Lee. Data-driven
765 blended equations of state for condensed-phase explosives. *Combustion Theory and*
766 *Modelling*, 25(3):413–435, 2021.
- 767 [34] Stephen A. Andrews and Andrew M. Fraser. Estimating Physics Models and Quantify-
768 ing Their Uncertainty Using Optimization With a Bayesian Objective Function. *Journal*
769 *of Verification, Validation and Uncertainty Quantification*, 4(1), 06 2019. 011002.
- 770 [35] Stephen A. Andrews, Jeffery A. Leiding, Jasper Thrussell, and Christopher Ticknor.
771 Calibration and uncertainty quantification for davis equation of state models for the high
772 explosive pbx 9501 products. *Propellants, Explosives, Pyrotechnics*, 49(2):e202300110,
773 2024.
- 774 [36] Beth A. Lindquist, Ryan B. Jadrach, Juampablo E. Heras Rivera, and Lucia I. Rondini.
775 Uncertainty quantification for high explosive reactant and product equations of state.
776 *Journal of Applied Physics*, 134(7):075102, 08 2023.
- 777 [37] Jason D. Bender, Oleg Schilling, Kumar S. Raman, Robert A. Managan, Britton J.
778 Olson, Sean R. Copeland, C. Leland Ellison, David J. Erskine, Channing M. Huntington,
779 Brandon E. Morgan, and et al. Simulation and flow physics of a shocked and reshocked
780 high-energy-density mixing layer. *Journal of Fluid Mechanics*, 915:A84, 2021.
- 781 [38] Dean L. Preston, Davis L. Tonks, and Duane C. Wallace. Model of plastic deformation
782 for extreme loading conditions. *Journal of Applied Physics*, 93(1):211–220, 2003.
- 783 [39] N. R. Barton, J. V. Bernier, R. Becker, A. Arsenlis, R. Cavallo, J. Marian, M. Rhee,
784 H.-S. Park, B. Remington, and R. T. Olson. A multi-scale strength model for extreme
785 loading conditions. *Journal of Applied Physics*, 109(7):073501, 2011.
- 786 [40] Luis A. Zepeda-Ruiz, Alexander Stukowski, Tomas Opperstrup, and Vasily V. Bulatov.
787 Probing the limits of metal plasticity with molecular dynamics simulations. *Nature*,
788 pages 1476–4687, 2017.
- 789 [41] A. C. F. Cocks and M. F. Ashby. Intergranular fracture during power-law creep under
790 multiaxial stresses. *Metal Science*, 14(8-9):395–402, 1980.
- 791 [42] John A Moore and Andrew Frasca. A comparison of Gurson and Cocks-Ashby porosity
792 kinetics and degradation functions. *International Journal of Fracture*, pages 1–16, 2021.

This is the author's peer reviewed, accepted manuscript. However, the online version of record will be different from this version once it has been copyedited and typeset.
PLEASE CITE THIS ARTICLE AS DOI: 10.1063/5.0226642

- 793 [43] N R Barton, M Rhee, S F Li, J V Bernier, M Kumar, J F Lind, and J F Bingert. Using
794 high energy diffraction microscopy to assess a model for microstructural sensitivity in
795 spall response. *Journal of Physics: Conference Series*, 500(11):112007, may 2014.
- 796 [44] Nathan Barton. Results from a new Cocks-Ashby style porosity model. *AIP Conference*
797 *Proceedings*, 1793(1):100029, 2017.
- 798 [45] S. B. Qamar, J. A. Moore, and N. R. Barton. A continuum damage approach to
799 spallation and the role of microinertia. *Journal of Applied Physics*, 131(8):085901, 2022.
- 800 [46] *Variational Bayesian Calibration of a PTW Material Strength Model for OFHC Copper*,
801 volume ASME 2023 Verification, Validation, and Uncertainty Quantification Symposi-
802 um of *Verification and Validation*, 05 2023.
- 803 [47] R. Becker. Ring fragmentation predictions using the Gurson model with material sta-
804 bility conditions as failure criteria. *International Journal of Solids and Structures*,
805 39(13):3555–3580, 2002.
- 806 [48] S Bastea and LE Fried. *Chemical Equilibrium Detonation*, volume 6. 2012.
- 807 [49] Joel G. Christenson, Laurence E. Fried, Sorin Bastea, Michael H. Nielsen, Trevor M.
808 Willey, and Michael Bagge-Hansen. The role of detonation condensates on the perfor-
809 mance of 1,3,5-triamino-2,4,6-trinitrobenzene (TATB) detonation. *Journal of Applied*
810 *Physics*, 132(9):095901, 09 2022.
- 811 [50] GPy. Gpy: A gaussian process framework in python. since 2012.
- 812 [51] Shuh Rong Chen and George T Gray. Constitutive behavior of tantalum and tantalum-
813 tungsten alloys. *Metallurgical and Materials Transactions A*, 27:2994–3006, 1996.
- 814 [52] PJ Maudlin, JF Bingert, JW House, and SR Chen. On the modeling of the taylor
815 cylinder impact test for orthotropic textured materials: experiments and simulations.
816 *International Journal of Plasticity*, 15(2):139–166, 1999.